UNDERWATER EXPERIMENTAL PLATFORM FOR STUDYING THE BEHAVIOR AND PERFORMANCE OF A SUBMERSIBLE PROPELLED BY A FLUID-CONVEYING FLUTTERING TAIL

By

Paul Christian Strefling

A THESIS

Submitted to
Michigan State University
in partial fulfillment of the requirements
for the degree of

MASTER OF SCIENCE

Mechanical Engineering

2011

ABSTRACT

UNDERWATER EXPERIMENTAL PLATFORM FOR STUDYING THE BEHAVIOR AND PERFORMANCE OF A SUBMERSIBLE PROPELLED BY A FLUID-CONVEYING FLUTTERING TAIL

By

Paul Christian Strefling

We have successfully designed and developed an underwater experimental platform for studying the dynamic behavior and performance of a novel submersible, which is propelled by the synergistic combination of jet action and oscillatory motion of a fluid-conveying flexible tail. The submersible, which we have named the Synergistically Propelled Ichthyoid, or SPI, ingests water through an orifice in its fore-body and expels it through a jet located at the rear end of the tail. The fluid flow through the flexible tail induces flutter instability and generates a traveling wave along the length of the tail. A single prime mover in the form of a pump is used for propulsion but the thrust is generated by the combination of jet action and jet-induced tail oscillations. The submersible has been designed to accommodate prime movers for propulsion and buoyancy control, sensors for feedback control, and active and passive fin assortments for maneuvering and stability. In addition, the submersible has a data acquisition system and on-board computing platform for autonomous and semi-autonomous operation. With over 30 hours of underwater testing we have converged on a design that is robust and dependable for further experimental research. This platform is ideally suited for investigating thrust and efficiency characteristics of the tail waveform for different tail designs and is expected to provide clues for design of rapid tail-assisted maneuvers.

```
if graduate_student(Ben_LeVesque,2015)[1]

     echo "This thesis is dedicated to Ben LeVesque in hopes that it
           will persuade him into perusing graduate school in the near future."

else

     echo "This thesis is dedicated to my loving family."

end
```

[1]Clearly $graduate\_student(name, year)$ is a function that can read into the future.

ACKNOWLEDGMENTS

I would like to thank all of those people who helped make this thesis possible.

First, I wish to thank Dr. Ranjan Mukherjee for the design freedom he allowed and encourage in regards to SPI. I am grateful that I was fortunate enough to work with him and look forward to working with him in the future. I would also like to thank Aren Hellum for his exceptional understanding of carangiform dynamics and overall fluids as a whole. He is a fluid mechanician on a Fossian scale.

I would like to thank my family for their continued support and their curiosity in regards to my research. Many thanks to Penniless Heiress and Rooftop Sy as well. Their lack of interest in engineering and overall common sense never fails to amuse me.

TABLE OF CONTENTS

List of Tables . . . . **vii**

List of Figures . . . . **viii**

Nomenclature **xi**

1 Introduction **1**
- 1.1 Motivation and Background of Submersibles 1
- 1.2 Propulsion by Fluid Conveying Fluttering Tails 3

2 Dynamic Model **7**

3 Mechanical Design **11**
- 3.1 Requirements 11
- 3.2 Hull Construction 12
  - 3.2.1 Nose Cone 15
  - 3.2.2 Tail Clamp 16
  - 3.2.3 Buoyancy Control 19
  - 3.2.4 Hydroplanes/Diving Planes 19
- 3.3 Prime Mover 22
- 3.4 Tail Construction 22
  - 3.4.1 Material Selection 23
  - 3.4.2 Fabrication 23

4 Computing Platform, Actuators, Sensors and Circuits **26**
- 4.1 Computing Platform Requirements 27
- 4.2 Pumps and Servos 27
- 4.3 Sensors 33
- 4.4 Microcontroller and Digital to Analog Converter 35
- 4.5 Wireless Interface 37
- 4.6 Power Supply 39

5 Software **41**
- 5.1 Introduction 41
- 5.2 Client Software 42
- 5.3 Wireless Encoding and Decoding 43
- 5.4 Microcontroller Software 45

6 Experimental Methods **47**
6.1 Introduction 47
6.2 Free Locomotion 49
6.3 Guided Locomotion 51

7 Experimental Results **53**

8 Future Improvements **57**

9 Conclusions and Future Research **60**

A Dynamic Model Literature Review **63**
A.1 Uniform Velocity Profile 63
A.2 Non-Uniform Velocity Profile 70

Bibliography **80**

LIST OF TABLES

3.1 Sample of acceptable materials for flexible tails. Note that current flexible tails have been constructed out of latex. 23

4.1 Specification of the HiTec HS-5056MG 30

4.2 Gyro Electrical Characteristics 34

4.3 Accelerometer Electrical Characteristics 34

5.1 Encoding and checksum values for the wireless algorithm. 45

7.1 Mean speeds of the three tested configurations in meters and body lengths per second for all runs performed to date. 54

7.2 Mean speeds of the three tested configurations in meters and body lengths per second for all submerged runs. 55

LIST OF FIGURES

1.1 The RoboTuna platform, on display at the Science Museum in London, was built by a team of researchers at the Massachusetts Institute of Technology (MIT) led by Michael Triantafyllou. David Barrett built the first RoboTuna known as Charlie I in 1995 for his PhD thesis. David Beal and Michael Sachinis, who introduced modifications including a cable-pulley system to produce RoboTuna II. Picture Credit: Science Museum/Science & Society Picture Library. For interpretation of the references to color in this and all other figures, the reader is referred to the electronic version of this thesis. . . 5

2.1 Neutral stability curves for different values on rigid body mass fraction μ from [23]. Regions to the left of the dotted line on each cure represent a region of negative thrust produced from the tail oscillations. 10

3.1 (a)-Two piece monocoque hull. (b)-Modular nose cone. (c)-20 AA NiMh Batteries. (d)-Rule Inline 500 GPH bilge pump. (e)-Dorsal Fin. (f)-Anal Fin. (g)-Tail Clamp. (h)-Charging and data port. (i)-External location of the charging and data port. 12

3.2 SPI's custom designed seal geometry includes a male/female interface that compresses a bead of silicon RTV as seen in the explosion in this figure. The silicon RTV is user replaceable and easy to inspect. 14

3.3 A cross section view of SPI's current nose cone. External sealing to the hull is accomplished with two silicone o-rings that live in the nose cone. The wetted surfaces of the nose cone are a continuation of the hull itself creating a smooth transaction into the orifice. 15

3.4 Exploded view of nose cone installation showing how the hull seal is routed around the centerline of the hull to avoid a three part interface resulting in a less complicated sealing interface. 17

3.5 An exploded view of the tail clamp showing the nozzle, hose barb and sealing features of the hull. 18

3.6 The SPI tail clamping mechanism. The set screws are used to clamp the sheet metal around the latex tail to ensure the clamped boundary condition. . . . 18

3.7 Two 120ml buoyancy tanks in fore (a) and aft (b) locations in the hull. These two buoyancy tanks can be used for static and dynamic depth control as well as static and dynamic rake. 20

3.8 Hydrofoils installed on SPI incorporating a symmetric design which has been chosen such that lift is not created at zero camber angles. This reduces unnecessary drag as static depth is controlled by the buoyancy chambers. (a) Isometric view of the hydrofoil location. (b) Cross section of the hydrofoil. (c) Plan view of the hydrofoil. 21

3.9 A swift and energetic Blacktip shark with its pectoral fins. These large, developed pectoral fins are used for dynamic depth control and aggressive trajectory control; the Blacktip shark has been known to launch itself out of the water and spin three to four times about its axis before returning to the water. Speed attained by the shark during these jumps has been estimated to average 6.3 m/s [39, 8]. This image was originally post to Flickr by StormyDog. *Shark*. 10 May 2011. http://flickr.com/photos/32184789@N00/134610871. . 21

3.10 Two manufacturing methods for creating latex flexible tails. (Top) a laminated tail that is held together with silicon RTV and placed in a two piece compression mold. (Bottom) a butt constructed tail that is also held together with silicon RTV. 24

3.11 The tail mold for flexible tails that are made using the laminated approach. Pins are used to ensure alignment between the two halves. 25

4.1 Circuit diagram of SPI's single direction motor driver. Where Q1 is the N-Channel MOSFET, D1 is the flyback diode, C1 acts as a filtering capacitor, R1 is a pull-down resistor and AGND is the circuits analog ground. 29

4.2 Circuit diagram of SPI's switching regulator for producing a clean 5 volts for the hydroplane servos. NOTE: Need to define F1,C2,R2,D3 and L1(or refer to spec sheet perhaps?). 30

4.3 Switch output source saturation versus source current for the MC34167 . . . 32

4.4 The SPI antenna which passes through the hull and extends 22.6 cm above the waterline. 38

4.5 An exploded NiMh cell as a result of a short in the system can be seen here. The chemical resistant heat shrink completely contained the failure protecting, SPI, the environment and personnel. 40

5.1 A high level flow chart that lays out the flow of communications from the user to SPI including the communications protocols and media that are used. . . 42

6.1 Three different tail geometries have been testing with the experimental platform. (Top) A rigid tail with identical geometry and buoyancy of a flexible tail. (Middle) A rigid tube that has the same length and fluid jet exit conditions as a corresponding rigid of flexible tail. (Bottom) The flexible tail, made of neutrally buoyant latex a constructed using the butt-welded method. . . 49

6.2 SPI testing under guide string conditions with a rigid tail. The guide strings only purpose is to provide a straight trajectory for SPI; power and communications are identical between free and guided locomotion. 52

7.1 High-speed images of the SPI acquired over a period of 1 sec, soon after it started from rest in the MSU swimming pool. The SPI was moving with an average speed of $\approx$ 0.4BL/s, less than the maximum speed of $\approx$1.15BL/s; note the large deflections of the tail which occur during acceleration. 54

7.2 Average speeds of the configurations listed in Table 7.1 which include 175 runs, with error bars denoting the limits of the 95% confidence intervals. Points denoted by a $\Box$ indicate runs which traveled North in direction while points denoted with a $\Diamond$ indicate runs in the opposite direction. 55

7.3 Average speeds of the configurations listed in Table 7.2 which were performed completely under the surface of the water totaling 60 runs. Error bars denoting the limits of the 95% confidence intervals, points denoted by a $\Box$ indicate runs which traveled North in direction while points denoted with a $\Diamond$ indicate runs in the opposite direction. 56

8.1 The proposed calibrated elbow that will provide SPI with the means necessary to provide a consistent flow rate to the tail regardless of the state of the power supply. 58

A.1 A fluid-conveying pipe and a magnified view of a small element along its length including the cross sectional dimensions. 65

A.2 Free-body diagram of (a) a fluid element and (b) its corresponding pipe element. 68

A.3 Cross sectional view of three concentric fluid volumes described by triple plug flow 71

Nomenclature

β_e nondimensional mass ratio for the external fluid

β_i nondimensional mass ratio for the internal fluid

λ nondimensional parametrization coefficient of rigid body's length

μ nondimensional parametrization coefficient of rigid body's mass

ψ_B nondimensional parametrization coefficient of rigid body's shape

E Young's Modulus (MPa)

I Area Moment of Inertia (m^4)

U Internal fluid velocity relative to the pipe (m/s)

u_e nondimensional external fluid velocity

u_i nondimensional internal fluid velocity

Chapter 1

Introduction

1.1 Motivation and Background of Submersibles

It is a well-known fact that 71% of the Earth's surface is covered by water; the majority of this water, approximately 97% is contained in the oceans. Oceans are the life blood of Earth, they drive the weather, regulate temperature and ultimately support life as we currently know it. It is imperative that we understand this aquatic ecosystem to ensure that it remains strong and resilient tomorrow as it does today. The oceans are a home to numerous life-forms, as it currently stands only 230,000 marine species have been identified, but it is estimated that over 2 million species exist. This is not surprising considering that only 5% of the ocean has been explored. Clearly there is a need for greater underwater exploration to obtain a better understanding of the most important ecosystem on earth.

It is not a trivial task to explore these vast bodies of water though. An efficient submersible platform that can withstand extreme pressures and cover great distances is needed. Ocean exploration from the surface of the water is significantly easier than doing so from below the surface; surface vessels existed for more than 10,000 years before the first submersible know as the Drebbel which was built in 1620. However, there are significant benefits from exploring the oceans at depth. The ability for real time control and quick maneuverability provide benefits to underwater exploration that can not be obtained from large surface vessels.

Underwater exploration has been greatly accelerated with the use of remotely operated underwater vehicles (ROVs) since the 1950s as the required technology to do so has been developed and perfected. Unmanned ROVs have several benefits compared to a manned platform such as "the relative economy of development in time and equipment costs, unlimited operational endurance on site by virtue of the cable link to the surface, surface control and coordination of project efforts, ability to perform in hazardous areas without endangering personnel, ability to change or modify all system components to meet individual tasks range needs without affecting system safety or certification status, and ease of changing crews without disrupting the mission." [45].

These benefits inspired Navy funded ROV's in the 1950s and 1960s for recovery of lost objects such as the missing hydrogen bomb from the 1966 Palomares B-52 crash. The hydrogen bomb, located by the manned DSV ALVIN submarine in 880 meters of water in the Mediterranean sea was recovered by an unmanned torpedo recovery vehicle known as the Cable-Controlled Underwater Recovery Vehicle or CURV-I [21]. Using technology for the CURV and CURV-like ROVs the oil and gas industry began deploying similar ROVs in offshore drilling platforms and pipelines in the 1980s as the depths exceeded the reach of human divers [10].

The academic and scientific communities have made substantial advancement in ROVs since the 1980s producing autonomous platforms, highly accurate underwater positioning systems, and an assortment of specialized tools for deep-sea tasks. Several key research institutions have pushed the design of submersibles with such accomplishments as the Woods Hole Oceanographic Institution's (WHOI) hybrid autonomous under water vehicle (HROV) Nereus[1], Jason, and Jason II. The Monterey Bay Aquarium Research Institute's (MBARI) fleet of ROVs including the Tiburon and Ventana and the University of Rhode Island's (URI) Hercules, all capable of advanced underwater functions that have made significant contributions to advancement of ROVs [14, 32].

Modern technology such as microcontrollers and high capacity batteries has enabled variations and improvements in submersible platforms including miniaturizations and platforms that have been developed for reasons other than object recovery or sea floor exploration. Such examples include alternative propulsion methods and autonomous algorithms for schools of robotic submersibles [9, 46]. These advanced platforms have gained the freedom of tether-less operation with technologies common in consumer electronics as well as complete underwater communications with technologies such as the WHOI micro-modem [15].

1.2 Propulsion by Fluid Conveying Fluttering Tails

Alternate methods of propulsion are not a new field of study even though the technology to support such endeavors is fairly young. The promise of highly efficient, fish-like propulsion has been a matter of academic interest since Gray's pioneering work in the 1930s. In a 1936 paper [16], Gray determined that the speed attained by a dolphin should require approx-

[1] In May 2009 the Nereus dove to the bottom of the deepest surveyed point in the global ocean known as the Challenger Deep, a small depression at the bottom of the Mariana Trench named in honor of the original Challenger expedition of 1872 [14]

imately seven times the power available to the animal, a situation that has been dubbed Gray's Paradox, albeit a paradox that has been resolved by later workers [13].

In his seminal 1960 paper, Lighthill [28] used slender body theory to approximate the effect of the pressure field surrounding the fish and was able to derive expressions approximating the thrust generated and power requirements of an idealized fish. Lighthill found that a traveling waveform with a phase velocity in excess of the fish's forward speed is required to produce efficient thrust and estimated that 90% of the power expended by a swimming fish is available (before consideration of viscous losses) to propel the fish; the remainder is wasted, serving only to raise the kinetic energy in the wake.

This predicted efficiency of this locomotion strategy provides a sound reason for robotic investigations into fishlike motion. A well-known biomimetic platform is MITs RoboTuna [4, 47], which uses an articulated tail covered by a tail-shaped sheath. The links which make up this tail are individually actuated in an approximation of a fish's motion. A different approach was taken by Alvarado and Youcef-Toumi [48], who described a system which used a wholly flexible tail, excited with a single actuator at the base. The fundamental difference between these approaches is that the RoboTuna's need to independently actuate the links of its articulated tail means that the system must essentially be driven against its natural dynamics, whereas Alvarado's flexible tail can be induced to oscillate near its natural frequency.

Compared to the literature produced on articulated mechanisms, work on flexible tails is relatively sparse. In addition to the aforementioned paper by Alvarado and Youcef- Toumi, an earlier attempt to design the type of propulsor we describe here was made by Païdoussis and coworkers in the mid-1970s [38]. Harper and coworkers [20] constructed an articulated

Figure 1.1: The RoboTuna platform, on display at the Science Museum in London, was built by a team of researchers at the Massachusetts Institute of Technology (MIT) led by Michael Triantafyllou. David Barrett built the first RoboTuna known as Charlie I in 1995 for his PhD thesis. David Beal and Michael Sachinis, who introduced modifications including a cable-pulley system to produce RoboTuna II. Picture Credit: Science Museum/Science & Society Picture Library. For interpretation of the references to color in this and all other figures, the reader is referred to the electronic version of this thesis.

tail, which was actuated in series with lateral and torsional springs so that the motion of the tail is under-actuated; this system represents a kind of intermediate form between the infinitely continuous beam-like tails and discrete systems. In this work, we propose a sort of flexible tail in which the desired traveling waveform is produced by flutter instability induced in a slender tail by conveying fluid down its center rather than by an actuator at the base. This instability is sometimes referred to as the garden hose instability, after the tendency of such a hose to whip about when the faucet is opened too far.

The Synergistically Propelled Ichthyoid (SPI) is our implementation of an underwater experimental platform to test propulsion by means of a fluttering tail. It is the third generation of devices that have been created for this purpose. However, this iteration of SPI presented in this paper differs considerably from previous designs as it includes numerous features that are unique to it and cannot be found on previous versions created here at Michigan State University or anywhere else in the academic community. In addition to its rich features, many aspects of SPI are based upon nature itself including an overall fish-like appearance with fin anatomy and curved aerodynamic surfaces often found in many species of carangiforms. Not only does SPI have features that are used in our testing today, provisions have been set forth for numerous features and additions for future needs. Equipped with data acquisition and a modular hull design this experimental platform has many opportunities for use in the development of fluttering tails as well as other submersible experimental testing.

Chapter 2

Dynamic Model

The concept behind propulsion by a fluttering tail is based on the natural locomotion of a carangiform and carangiform-like animals that swim by oscillatory movement of their posterior end. This movement, most notably the side-to-side motion of the caudal fin produces a thrust which propels the animal in the forward direction. In the case of SPI, flutter instability is induced by conveying fluid through a tube that forces the tail to oscillate and generate a traveling wave, which provides a forward thrust in a similar means to that of a fish. Forward thrust is provided by the oscillating tail as well as the fluid jet that exits the end of the fluid-conveying pipe. The analysis of thrust from a fluid-conveying pipe will begin by considering the pipe and the pipe only. Consider a pipe that is sufficiently flexible such that it begins to flutter as the flow rate of the fluid increases. Whether the pipe is fluttering or not, the exit conditions of the pipe are equivalent to that of a jet or nozzle that results in thrust from the fluid jet.

For the SPI, the jet thrust will cause an acceleration in the direction opposite of the jet. This jet will drive SPI to a velocity in which the drag forces match that of the jet force and the platform reaches an equilibrium velocity. As the flow rate increases and the flexible pipe begins to flutter, the forward trust provided from the jet will no longer be parallel to the center-line of the hull for all instances of time. As the tail flutters back and forth, the exit angle of the jet will pass through a range of angles that will still contribute to thrust in the forward direction. The vectoring of the jet due to flutter will result in a loss of thrust in comparison to a straight jet. However, the oscillatory motion of the tail mimics the traveling wave found in powerful carangiforms suggesting that further investigation may find that exceeding the efficiency of a standalone jet is possible. The SPI experimental platform has been developed to study this phenomenon and help answer questions of feasibility and efficiency, and investigate the possibility of developing control strategies that can provide turning capability.

A complete review of the literature pertaining to the theory and experimentation of fluid conveying tubes beginning in 1878 is included in Appendix A. Which also details the development of the equations presented in this chapter.

Theoretical development of the dynamic model that captures the instabilities of a fluttering tail and the thrust produced by the oscillations has been investigated by Hellum and Mukherjee [22, 23]. Based on the work presented in [23] the equation of motion for a fluid-conveying fluid immersed pipe is even by

$$Y'''' + \left(u_i^2 + u_e^2\right) Y'' + 2\left(u_i\sqrt{\beta_i} + u_e\sqrt{\beta_e}\right)\dot{Y} + \ddot{Y} = 0 \tag{2.1}$$

where u_i and u_e are the non-dimensional internal and external velocities respectively, and β_i and β_e are the nondimensional mass ratios for the internal and external fluid respectively. The non-dimensional linearized boundary conditions for the tail with a clamped interface with the rigid body represented at ($X = 0$) are given by [23]

$$[Y''' + \mu(\ddot{Y} - \lambda\dot{Y}')]_{X=0} = 0 \tag{2.2}$$

$$[Y'' - \mu(\psi_B + \lambda^2)\ddot{Y}' - \lambda\ddot{Y}]_{X=0} = 0 \tag{2.3}$$

$$Y''(1) = 0 \tag{2.4}$$

$$Y'''(1) = 0 \tag{2.5}$$

where the nondimensional coefficients ψ_B, λ, and μ parametrize the shape, length and mass of the rigid body. Eqs.(2.4) and (2.5) provid the boundary conditions of the free end.

Eqs.(2.1), (2.2), (2.3), (2.4) and (2.5) can be solved to obtain an expression for $Y(X,T)$,

$$Y(X,T) = \sum_{n=1}^{4} A_n e^{z_n X} e^{i\omega T} = \sum_{n=1}^{4} A_n \underbrace{e^{\Re[Z_n]X}}_{\text{(i)}} \underbrace{e^{i(\Im[Z_n]X + \Re[\omega]T)}}_{\text{(ii)}} \underbrace{e^{-\Im[\omega]T}}_{\text{(iii)}}. \tag{2.6}$$

which captures the the transverse deflection of the tail. Inspecting Eq.(2.6) indicates that $Y(X,T)$ is a product of three exponential terms, (i), (ii) and (iii). The first term, $e^{\Re[Z_n]X}$ is bounded since X is bounded. The second term, $e^{i(\Im[Z_n]X+\Re[\omega]T)}$ is oscillatory from its imaginary exponent. The third term, $e^{-\Im[\omega]T}$ can grow unbounded with time if $\Im[\omega] < 0$ which represents the unstable dynamics of the pipe. The exact mode and the velocity at which the fluid-conveying pipe becomes unstable depends on the fluid mass fraction β which is explained in detail in [23].

The stability boundaries for a fluid-conveying fluttering tail can be seen in Fig.2.1 which is an Argand diagram for various values of μ, the mass of the rigid head. The value of $\mu = \inf$ represents a cantilever while $\mu = 0$ represents a free end. The dotted line through

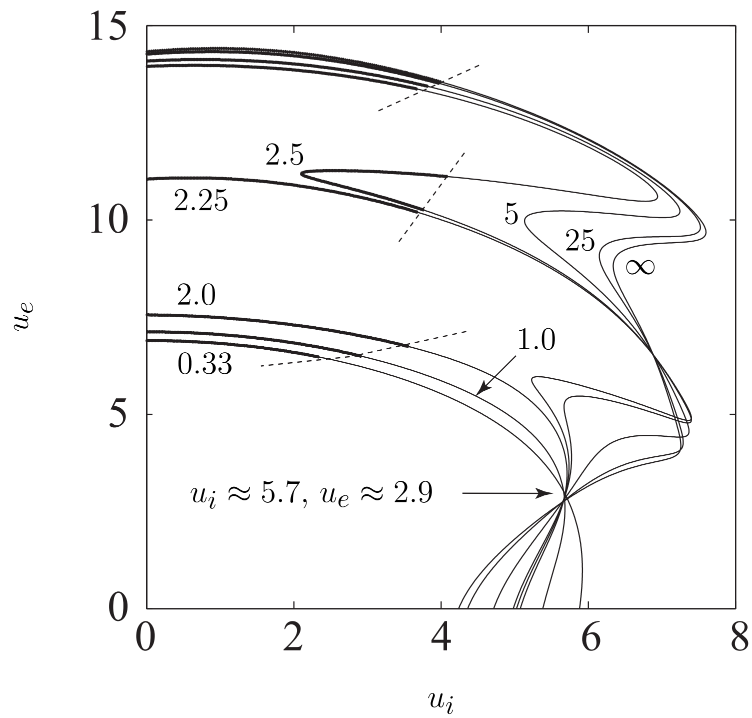

Figure 2.1: Neutral stability curves for different values on rigid body mass fraction μ from [23]. Regions to the left of the dotted line on each cure represent a region of negative thrust produced from the tail oscillations.

each curve represents the transition point at which a fluttering tail provides negative and positive thrust. Left of the dotted line, a curve represented in bold is an area in which it is predicted that the tail oscillations will produce a negative thrust. Curves to the right of the dotted line represent areas in which it is predicted that tail oscillations will provide positive thrust. However, even in the event that tail oscillations produce negative thrust, the synergistic action of the tail allows the fluid jet to maintain bias towards positive thrust.

Based on the work in [23] and the inspiration of fish-like efficiency it was proposed that if we were to implement a submersible with a fluid-conveying fluttering tail that it would potentially outperform a fluid jet of the same geometry. With this goal, we set forth to design an experimental platform to quantify the performance of a fluid-conveying fluttering tail.

Chapter 3

Mechanical Design

3.1 Requirements

We have developed a modular design to develop the SPI experimental platform to satisfy as many current and future requirements as possible. The general requirements for the mechanical design are to maintain buoyancy, provide housing for both mechanical and electronic components, as well as to remain dry under all testing conditions including situations resulting in impacts and extended periods of time on the bottom of the pool. In addition to these general requirements, the modular design allows most components to be easily updated or replaced to accommodate design or experimental changes and/or requirements without the need for a complete redesign of the platform. For example, fin geometry including the tail fin, pectoral fins, dorsal fin and anal fin are independent of the main hull and can all be modified and installed without the need for hull modifications.

The primary mechanical components of SPI, both internal and external are introduced and labelled in Fig.3.1. With the exception of the Rule inline 500 gallon per hour (GPH)

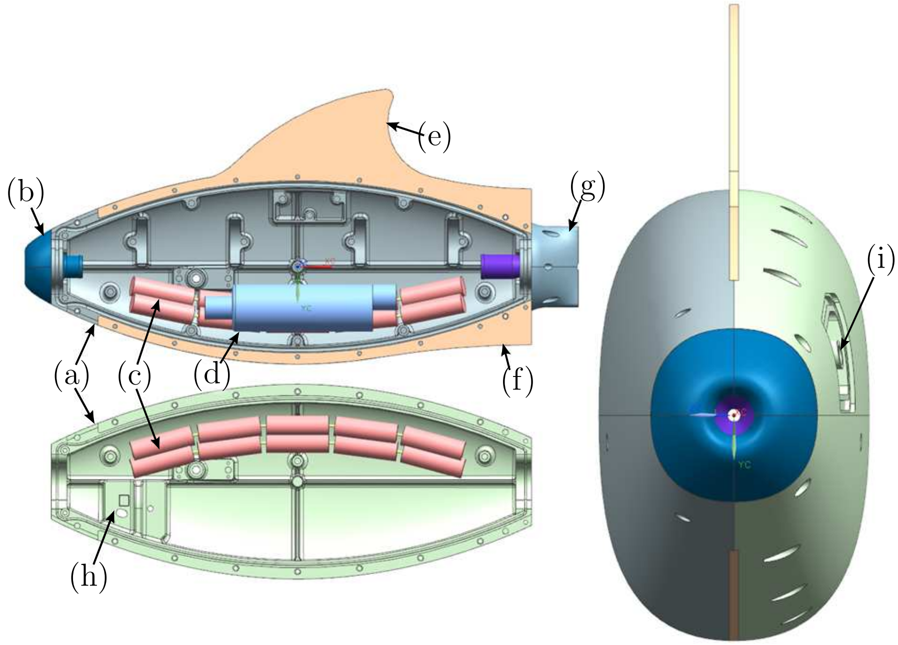

Figure 3.1: (a)-Two piece monocoque hull. (b)-Modular nose cone. (c)-20 AA NiMh Batteries. (d)-Rule Inline 500 GPH bilge pump. (e)-Dorsal Fin. (f)-Anal Fin. (g)-Tail Clamp. (h)-Charging and data port. (i)-External location of the charging and data port.

bilge pump and the array of NiMh batteries, all of the components represented in the figure have been custom-designed and manufactured for the SPI experimental platform. These components and, specifically, the hull have been designed to be as universal as possible to reduce the need for design iterations and additional manufacturing.

3.2 Hull Construction

The hull of the SPI is machined from Delrin (Polyoxymethylene) to form two major monocoque halves to create a water tight enclosure. A monocoque design was chosen to simplify the design and mounting of the various components that live inside the hull. Mounting features that have been designed into the hull include the necessary geometry and mounting features to accurately and easily incorporate 20 AA batteries; a 500 gallon per hour pump;

two large, 60ml ballast tanks with independent pressure pumps; as well as two hydroplanes including their servo motors. The hull also has significant room for electronics and sensors, which currently include a custom designed circuit board equipped with a microcontroller, an Attitude Heading Reference System/Inertial Measuring Unit (AHRS/IMU), data logging capabilities, and other specialty sensors. The hull has also been machined with provisions for static semi-permanent ballast in the form of highly dense materials such as lead or tungsten.

To ensure a robust and dependable water tight enclosure the hull incorporates a custom designed sealing flange that is easily to inspect, maintain, and replace if damaged. The hull is split down the middle longitudinally to create two halves, specifically a left and a right. The halves have four 3/16" stainless steel dowels to ensure proper alignment and is fastened together with 18 6-32 stainless steel cap screws at approximately every 2 inches. The large population of fastening screws ensure that there is a consistent and uniform compression on the sealing surface removing the possibilities of local hull deformation, which may result in a breach of the hull at the seal interface. The seal geometry includes a male/female interface as seen in Fig. 3.2 that compresses a bead of silicon RTV (Room Temperature Vulcanization) to create a water tight seal in a similar method to an o-ring design.

The monocoque design incorporates bolting locations that have been designed into the hull to allow for various components to be fastened to the hull without the need for nuts, nut plates, or through hole designs. To add thread strength and robustness, all threaded holes have marine grade brass inserts to distribute the load over a larger shear area to reduce the chance of fastener pull out from accidental over torquing or highly stressed components. These inserts are available in three different diametrical sizes, each size increasing the shear area and permissible fastener tension. In the event of insert pull out the next size insert

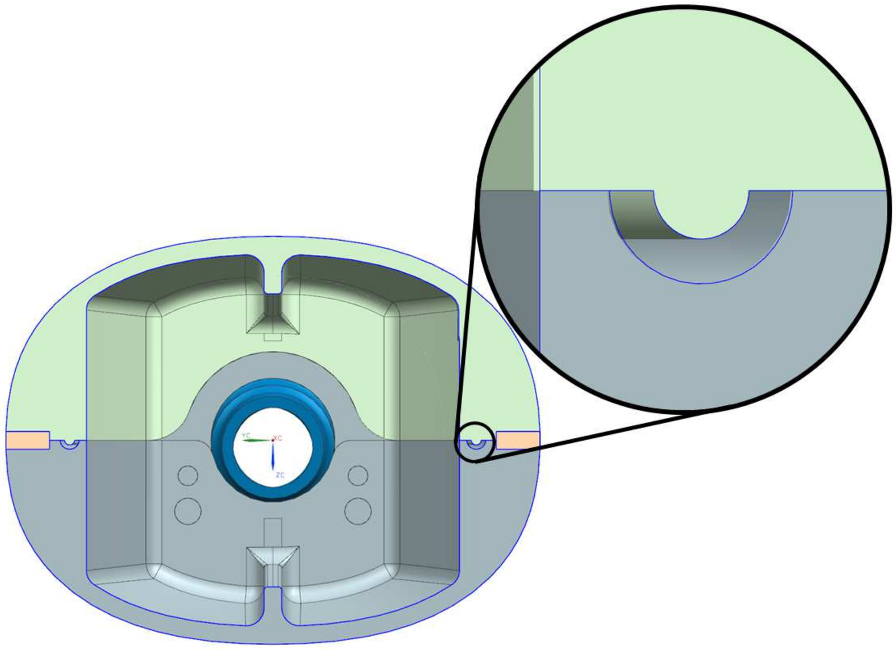

Figure 3.2: SPI's custom designed seal geometry includes a male/female interface that compresses a bead of silicon RTV as seen in the explosion in this figure. The silicon RTV is user replaceable and easy to inspect.

can be installed in the hull without the need to repair the damages with sub-par methods such as glues or epoxies that can not provide a sound and secure fastening method for an extended period of time.

The monocoque has been designed to be as modular as possible. Many design features have been included into this hull in hopes that it will be in service for many years because it can be adopted to fit many different testing scenarios. Not only is the hull designed for the evaluation of propulsion by fluttering tail, it can easily be updated to use other forms of locomotion without a complete redesign of the hull itself. Included in the modular design is the possibility to change nose cones, tail mounting, buoyancy tanks, as well as hydroplanes and the entire assortment of fins. The hull is not built for a specific internal pump either; it has been designed to accommodate a variety of pump geometries and sizes.

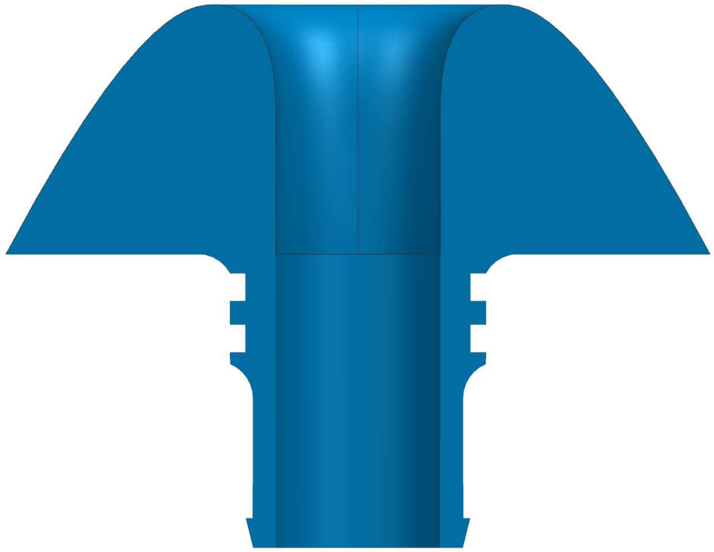

Figure 3.3: A cross section view of SPI's current nose cone. External sealing to the hull is accomplished with two silicone o-rings that live in the nose cone. The wetted surfaces of the nose cone are a continuation of the hull itself creating a smooth transaction into the orifice.

3.2.1 Nose Cone

The nose cone of the SPI is designed for two purposes, the first is to maintain a smooth transition from itself to the body. It has been modeled as a continuation of the hull itself and maintains tangency in all three dimensions. The second purpose of the nose cone is to provide a smooth inlet to the pump reducing pump losses. A cross section of the nose cone can be seen in Fig.3.3, which shows the tangency that has been maintained between the hull and the inlet. In addition to these surface features the nose cone also provides sealing geometry in the form of o-ring grooves for the external seal as well as a barbed fitting for the internal plumbing to the prime mover. The internal plumbing is composed of a silicon hose that bridges the connection between the nose cone and the pump. Internal seals are maintained by compressing the silicon hose onto the barb with a low profile pinch or "ear" stainless steel hose clamp.

To avoid a three part interface between the two sides of the hull and the nose cone, the sealing surface has been routed around the nose cone as seen in Fig.3.4, rather than maintained at the centerline of the hull as it does around the remainder of the perimeter, excluding the nozzle exit. This design decision has been made because it would be impossible to incorporate a compression seal between three surfaces without administering uncured silicon sealant during the assembly procedure. Although applying silicon sealant during assembly would most likely maintain a water tight seal, it is not, however, a feasible solution for an experimental platform because curing times are on the order of days when quick adjustments need to be made during testing sessions that have a duration of 1-2 hours. The current solution, as presented in Fig. 3.4 has proven to be robust and leak free with over 30 hours of underwater testing since the initial swim of SPI . Notice in the figure that the additional component shown in gold could have been incorporated into the design of the hull itself. However, by designing it as a separate component, it reduced the price of the hull material by a significant amount without greatly complicating the design. It can also be changed to allow for a larger diameter entrance if desired.

3.2.2 Tail Clamp

The tail clamp has identical sealing features as seen in the nose cone with the exception that it is a two-piece design that gives the user the ability to change the nozzle geometry or the tail clamp mechanism without having to redesign both pieces. The tail clamp itself does not provide any sealing features and is strictly used to provide the boundary conditions for the flexible tail and to remain as aerodynamic as possible. The tail clamp has been designed to enable tails to be quickly changed with minimal effort and minimal strain on the tail while providing features to reproduce tail boundary conditions during testing sessions and

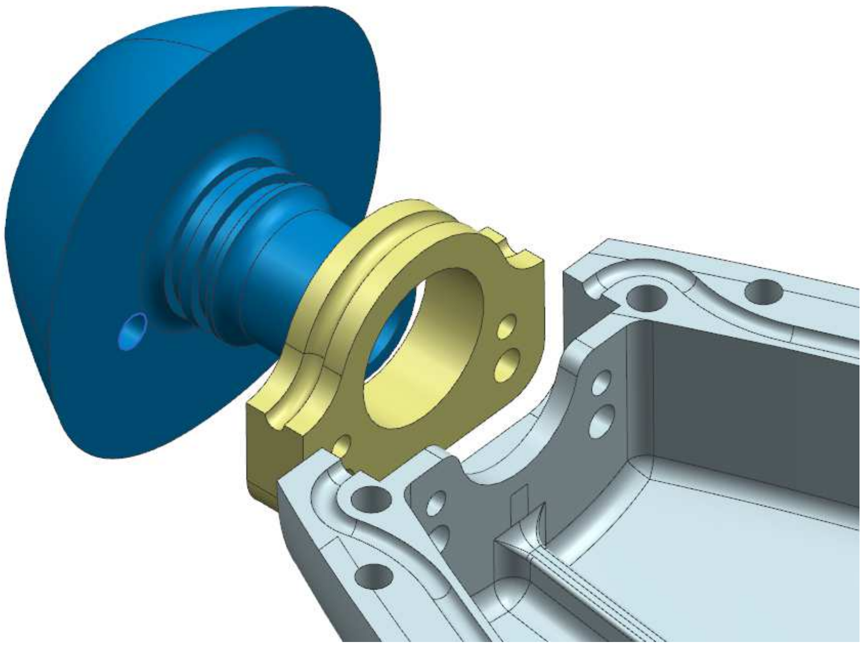

Figure 3.4: Exploded view of nose cone installation showing how the hull seal is routed around the centerline of the hull to avoid a three part interface resulting in a less complicated sealing interface.

throughout the lifetime of SPI.

Tails are "clamped" into the tail clamp by two stainless steel set screws that can be seen in Fig. 3.6, which provide a compressive force on the two stainless steel sheets that pinch the latex tail into the clamp and provide the desired boundary condition. The 5/16" ID latex tube extends towards the hull from the stainless steel pinch clamps and interfaces with the hose barb on the nozzle creating a leak proof seal to the high flow-rate nozzle. The pinch clamps not only provide the boundary condition for the tail, they also provide the necessary restraint to keep the tail hose from slipping off the barbed nozzle.

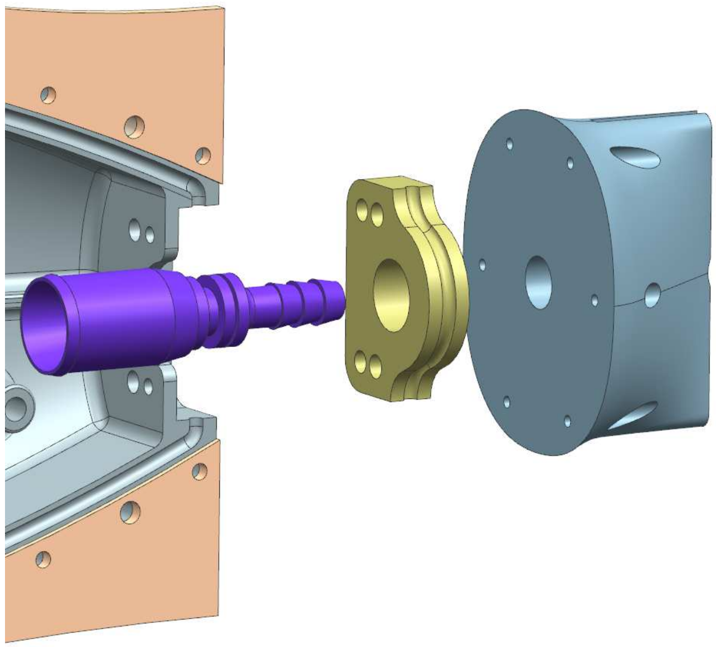

Figure 3.5: An exploded view of the tail clamp showing the nozzle, hose barb and sealing features of the hull.

Figure 3.6: The SPI tail clamping mechanism. The set screws are used to clamp the sheet metal around the latex tail to ensure the clamped boundary condition.

3.2.3 Buoyancy Control

The SPI has been designed to incorporate buoyancy tanks to maintain depth without a forward velocity. Two tanks as seen in Fig. 3.7 totaling 120 ml of capacity are strategically placed not to interfere with future pump changes or upgrades. The buoyancy system, which has not yet been installed, will be implemented such that each tank is independently operated to statically adjust the fore/aft CG without having to open the hull and manually place the mass. Independent buoyancy tank control is an important feature when tails are often switched as current tails are not neutrally buoyant to the degree that small changes in tail size do not effect the static rake of the hull. It is also worth mentioning that tailless performance and rigid tail performance measurements currently require the movement of the CG to maintain proper rake for both hydrodynamic and stability reasons. Externally controlling the hull's static rake is a beneficial feature that once implemented will greatly reduce experimental setup time, accuracy, and understanding. The details of the hydraulics of the buoyancy system have not been finalized at the time of this writing.

3.2.4 Hydroplanes/Diving Planes

The SPI has been designed to incorporate two hydroplanes or diving planes, one on each side of the hull biased towards the nose as seen in Fig. 3.8. Hydroplanes are typically found on submarines to assist the vehicle's pitch requirements and depth control at speed. When compared to the autonomy of a carangiform, hydroplanes are most similar to the pectoral fins as seen on the Blacktip Reef shark in Fig. 3.9. Highly developed pectoral fins, such as those found on sharks, are used for dynamic lifting for depth control as well as aggressive trajectory control [39, 8]. Dynamic lift is necessary for species that do not have the means

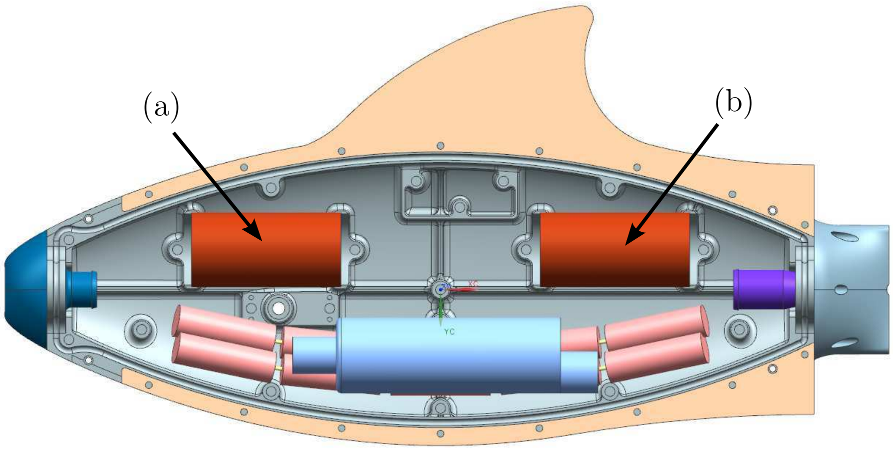

Figure 3.7: Two 120ml buoyancy tanks in fore (a) and aft (b) locations in the hull. These two buoyancy tanks can be used for static and dynamic depth control as well as static and dynamic rake.

of changing their buoyancy, or changing their buoyancy quickly. Many deep sea sharks have an oil rich liver to maintain the desired buoyancy, but to change depth quickly they rely on the dynamic lift associated with their pectoral fins.

SPI has incorporated hydroplanes for both depth control and yaw control similar to that of species of fish with highly developed pectoral fins. Unlike fish that depend solely on dynamic lift to maintain depth, SPI's primary depth control is achieved from the ballast tanks while the hydroplanes or pectoral fins are used for quick navigation changes. This allows SPI to maintain a depth without a forward velocity that would be required if depth control was maintained by the hydroplanes alone.

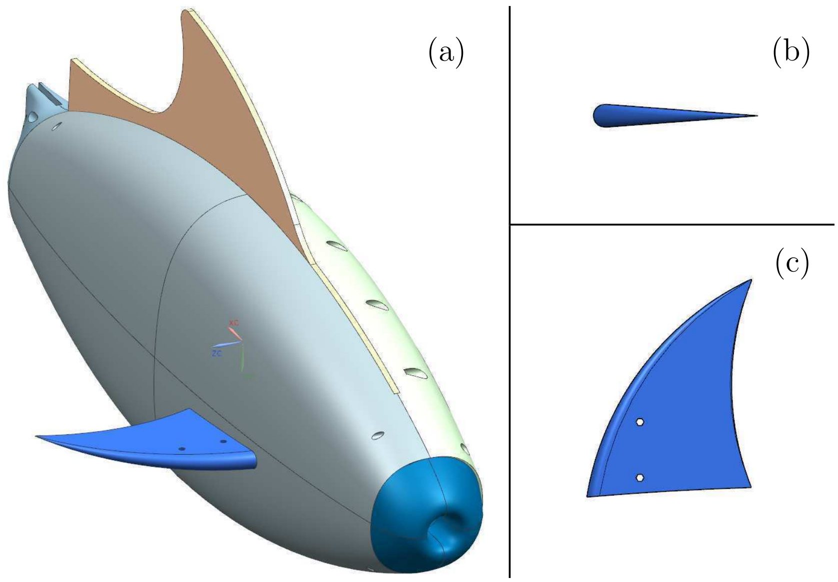

Figure 3.8: Hydrofoils installed on SPI incorporating a symmetric design which has been chosen such that lift is not created at zero camber angles. This reduces unnecessary drag as static depth is controlled by the buoyancy chambers. (a) Isometric view of the hydrofoil location. (b) Cross section of the hydrofoil. (c) Plan view of the hydrofoil.

Figure 3.9: A swift and energetic Blacktip shark with its pectoral fins. These large, developed pectoral fins are used for dynamic depth control and aggressive trajectory control; the Blacktip shark has been known to launch itself out of the water and spin three to four times about its axis before returning to the water. Speed attained by the shark during these jumps has been estimated to average 6.3 m/s [39, 8]. This image was originally post to Flickr by StormyDog. *Shark*. 10 May 2011. http://flickr.com/photos/32184789@N00/134610871.

3.3 Prime Mover

SPI's current prime mover for propulsion is the Rule iL500PK, a 500 Gallon Per Hour (GPH) marine inline submersible pump designed to run on a 12 volt system. It is an off-the-shelf part that is unmodified except for the addition of a fly-back diode and a large 1000 μF capacitor on the leads to reduce unwanted dynamics and noise from the motor. It is designed for continuous operation and has proven to be robust even when exceeding the manufacturer's recommended voltages for extended periods of time.

The Rule iL500PK is a centrifugal type pump that drives a plastic impeller at the inlet of the housing and exhausts the pumped water over the electric motor providing necessary and sufficient cooling for continuous operation. Current flow restrictions limit the pump to a maximum of 200 GPH.

3.4 Tail Construction

SPI's flexible tails needs to be sufficiently flexible to allow for fluttering behavior given the conditions imposed from the pump and its external velocity. Tail flexibility can easily be controlled with the combination of tail thickness and material properties. Tail knowledge is currently heavily based on experimentation that has found tails with a second moment of area of $5.6497e-10m^4$ with a Youngs Modulus of $900KPa$to be sufficient to sustain flutter. Tail buoyancy is also a factor that needs to be controlled to ensure proper hull dynamics. Tails deviating from neutrally buoyant will cause static rake in the hull; which results in surfacing, diving, and bobbing instabilities when under power. For example, a heavier-than-water tail can cause the tail to droop behind the hull and the entire platform may behave

Table 3.1: Sample of acceptable materials for flexible tails. Note that current flexible tails have been constructed out of latex.

Material	Specific Gravity	100% Modulus psi	Shore A Durometer Hardness
Latex	0.935	130	40
Evoprene	1	174-247	35
C-Flex	0.9	100-290	30-48
Softflex	.947-.972	102-290	31-50
Silastic	.930-.960	145-247	37-48
Dynaflex	.910-1.10	110-360	30-37
Elastamax XL	.9-1.1	98-487	34-48
Nexprene	.93-.94	131-139	36-45
Dryflex	1.04-1.08	102-290	30-50
Geniomer	.98-1.0	87-290	40-55

in an unpredictable manner.

3.4.1 Material Selection

Several materials have been found that fit both the stiffness and buoyancy requirements for tails with a nominal thickness of 1/20 of an inch. Acceptable materials can be found in Table 3.1. As seen in the table, several materials are sufficient candidates for feasible tails. However, current tails have been chosen to be fabricated from natural latex; it is highly available in a variety of thicknesses and can easily be fabricated into composite shapes as detailed in the following section.

3.4.2 Fabrication

Tail fabrication consists of a composite design where latex components are adhered to other latex components with Silicone Room Temperature Vulcanization (RTV). Current manufacturing methods include a laminated approach that can be seen in the top of Fig. 3.10 and a butt construction as seen in the bottom of Fig. 3.10. Both methods take a considerable

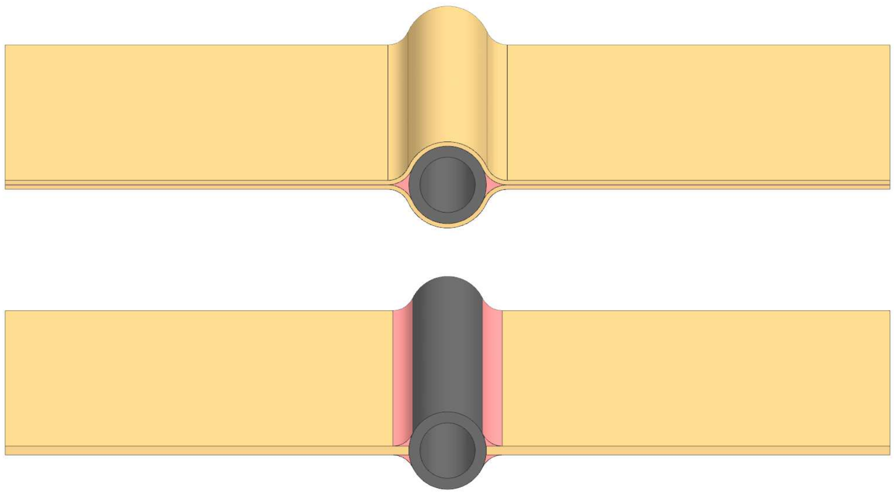

Figure 3.10: Two manufacturing methods for creating latex flexible tails. (Top) a laminated tail that is held together with silicon RTV and placed in a two piece compression mold. (Bottom) a butt constructed tail that is also held together with silicon RTV.

amount of time and a skilled and patient individual.

The butt construction is the simplest of the two and requires only a small fixture to assure that the tail sheet is in the center of the tail tube. Once centered a small bead of silicon is introduced to the seam and allowed to dry. This silicon can be seen in Fig. 3.10 with a salmon color. The laminated construction is similar to that of a composite wet layup used for fiberglass, carbon fiber, and Kevlar fabrication. Each internal surface of the tail is coated with a thin layer of low viscosity silicon, placed in a mold, and then clamped as seen in Fig. 3.11. Currently it has been found that laminated construction methods induces strain into the latex during the mold clamping period resulting in a permanent set. The permanent set is detrimental to tail performance resulting in current tails being produced with the butt construction method.

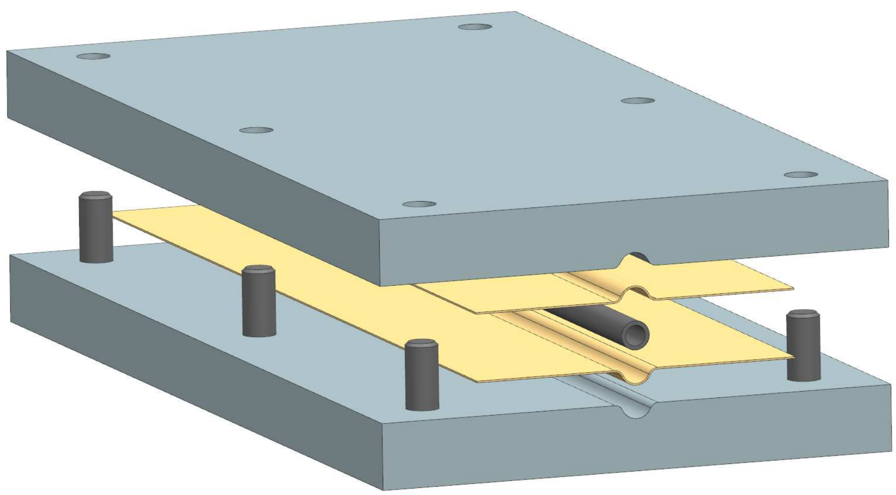

Figure 3.11: The tail mold for flexible tails that are made using the laminated approach. Pins are used to ensure alignment between the two halves.

Chapter 4

Computing Platform, Actuators, Sensors and Circuits

Acronyms and Abbreviations

ADC	Analog to Digital Converter
AHRS	Attitude Heading Reference System
AVR	Atmel AVR, a family of microcontrollers
GCC	GNU Compiler Collection, and open source compiler
IMU	Inertial Measuring Unit
MOSFET	MetalOxideSemiconductor Field-Effect Transistor
PCB	Printed Circuit Board
RDS	Resistance Drain-Source for MOSFETs
RISC	Reduced Instruction Set Computing
SD	Secure Digital Card, used for data storage
SPIB	Serial Peripheral Interface Bus, known as SPI outside of this document
UART	Universal asynchronous receiver/transmitter
USART	Universal synchronous/asynchronous receiver/transmitter
WHOI	Woods Hole Oceanographic Institution

4.1 Computing Platform Requirements

The requirements for the on-board computing platform are primarily to facilitate communication between the platform and the shore or dock and to execute multiple control algorithms in real time. In addition to these requirements, a design was sought to provide data acquisition and semi-autonomous decisions. Furthermore, it was crucial for the system to be inexpensive. Using an off-the-shelf miniature computer or other expensive all-in-one solutions were not feasible for a device that is deployed int a highly conductive chlorine environment. Even though many provisions have been set forth to minimize the possibility of a breach in the hull, it is still a significant threat and not worth the risk for a prototype device that has not been field tested for extended periods of time. To maintain a reasonable cost for possible replacement, a microcontroller was sought for its abundant set of features, versatility, and real-time computing environment. In addition to being inexpensive, the computing platform needed to have the ability to drive several brushed DC motors, control servo motors, and have the ability to run an Analog to Digital Converter (ADC).

4.2 Pumps and Servos

The Rule iL500PK is an centrifugal type pump that drives a plastic impeller pumping water in the same direction, regardless of the polarity of the terminals[1]. This characteristic, which is common with all the pumps we have currently considered does not require the need for the complex circuitry of an H-Bridge to reverse the polarity of the pump's driving circuit. To simplify the driving circuitry an N-Channel MOSFET was selected as a robust, and

[1]The intended pumping direction is more efficient than the opposite direction given the biased impeller design for centrifugal type pumps

inexpensive solution for the motor driver. This solution provides precise throttling ability and virtually no rejected heat with an internal Resistance Drain-Source (RDS) in the MOSFET of only 0.0095 Ω.

The Logic Level N-Channel MOSFET operates at battery voltage with a pulse width modulation (PWM) signal from the microcontroller operating on the gate of the MOSFET. The PWM signal operating on the oxide-insulated gate of the MOSFET induces a conducting channel between the source and the drain located on the MOSFET. In our application the source is connected to the system ground and the drain is connected on the negative terminal of the driving pump. This setup can be seen in Fig. 4.1, which shows the N-Channel MOSFET (Q1) and its supporting components including the PWM signal from the microcontroller as OC0. In this configuration the 100 kΩ pull-down resistor (R1) provides a path to ground for the gate in the event that the microcontroller fails to do so, such as a microcontroller restarting event. Without the pull-down resistor tying the gate to ground the MOSFET has the potential to drift creating a conducting channel between the source and the drain turning the pump on when it is not desired to do so. The diode (D1) in this circuit, often referred to as a flyback diode provides a path to effectively eliminate the sudden voltage spike from the inductive load of the pump when its supply voltage is reduced or removed. Capacitance (C1) in this circuit provides noise filtration from motor operation, C1 is on the order of 1000 μF. The Rule iL500PK, as purchased, has capacitance between its terminals inside the motor housing on the order of 0.1 μF, which removes a sufficient amount of higher frequency noise.

SPI's two hydroplanes are controlled with standard hobby-grade digital servos. Manufactured by HiTec, California, the 5056MG is a "mini" sized servo with a full metal gear train

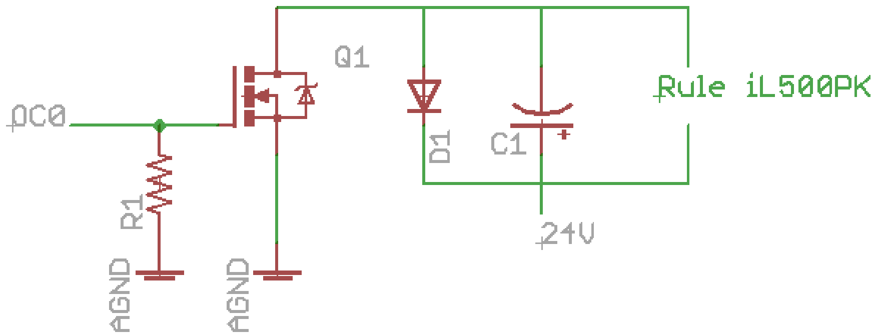

Figure 4.1: Circuit diagram of SPI's single direction motor driver. Where Q1 is the N-Channel MOSFET, D1 is the flyback diode, C1 acts as a filtering capacitor, R1 is a pull-down resistor and AGND is the circuits analog ground.

with ball bearing support. Its specifications can be seen in Table 4.1. The 5056MG's small size and relatively high torque output is an affordable and robust solution for the pectoral fins, which do not require high rotational resolution or excessive torque that can be found in more expensive alternatives to the hobby servo.

The 5056MG, like all HiTec servos, operates between 4.8 and 6 volts, which is not directly available from SPI's 24 volt battery pack. To provide a stable and robust voltage source for the servos, a switching voltage regulator was chosen to provide a clean and consistent voltage for the servos while maintaining a high efficiency that would otherwise be wasted as excess heat by a linear regulator. The power circuitry can be seen in Fig.4.2, which is based around *ON Semiconductor's* MC34167 5.0 Amp step-down switching regulator.

As specified from *ON Semiconductor*, the diode (D2) on the output of the switching regulator is a 1N5825 high frequency Schottky barrier rectifier specifically designed for low voltage high frequency circuits. The inductor (L1) on the output is specific to the application

Table 4.1: Specification of the HiTec HS-5056MG

Motor Type:	3 Pole
Bearing Type:	Top Ball Bearing
Speed (4.8V/6.0V):	0.11 / 0.09
Torque oz./in. (4.8V/6.0V):	21/25
Torque kg./cm. (4.8V/6.0V):	1.5 / 1.8
Size in Inches:	0.88 x 0.45 x 0.94
Size in Millimeters:	22.35 x 11.43 x 23.88
Weight ounces:	0.45
Weight grams:	12.76
Voltage V:	4.8 - 6
Pulse Voltage V:	3 - 5
Pulse Duration mS:	0.9 - 2.1, 1.5 Center

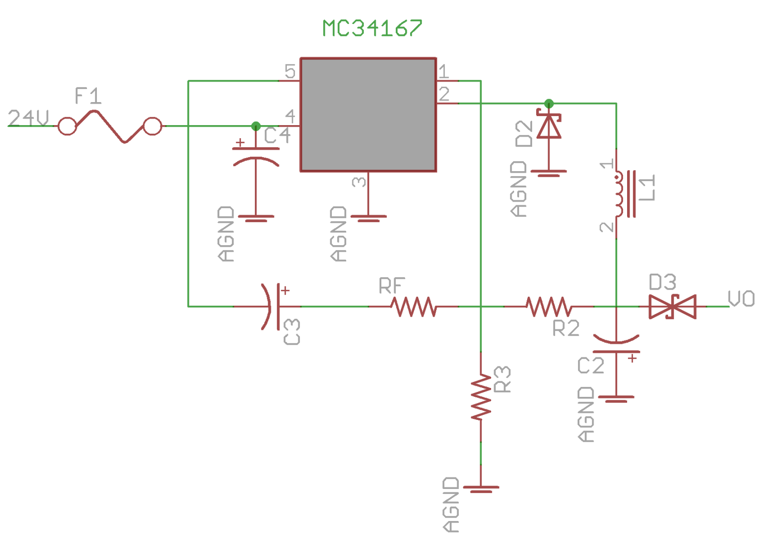

Figure 4.2: Circuit diagram of SPI's switching regulator for producing a clean 5 volts for the hydroplane servos. NOTE: Need to define F1,C2,R2,D3 and L1(or refer to spec sheet perhaps?).

and can be determined using step-down regulator design equations [41]

$$L = \left(\frac{V_{in} - V_{sat} - V_{out}}{\Delta I_L}\right) t_{on} \tag{4.1}$$

where V_{in} is approximately 24 volts, V_{sat} is determined from Fig.4.3, resulting in approximately -1 volts under heavy load, V_{out} is currently set at 5.0 volts to satisfy the input requirements of the servos, ΔI_L is the desired peak-to-peak inductor ripple current and can be set at twice the output current and $\Delta I_L = 2(I_{out})$. In Eq.(4.1), t_{on} is given by the expression

$$t_{on} = \frac{\alpha}{f_{osc}\,(\alpha + 1)} \tag{4.2}$$

where f_{osc} is the oscillator frequency of 72 kHz and α is defined as

$$\alpha = t_{on}/t_{off} = \frac{V_{out} + V_F}{V_{in} - V_{sat} - V_{out}} \tag{4.3}$$

where V_F is the output rectifier forward voltage drop which is 0.35 V for the 1N5822.

Setting R2 and RF at 6.8 kΩ and 68 kΩ respectively the MC34167 outputs 5.05 volts, which satisfies the input voltage requirements of the servos. However, initial testing of the servos was performed at 6.0 volts by computing R3 from the relation

$$V_{out} = V_{ref}\left(\frac{R2}{R3} + 1\right) \tag{4.4}$$

which equated to an R3 value of 36 kΩ using 5.05 volts as V_{ref}. Running the servos at 6.0 volts was however abandoned when the switching regulator failed. As a result of chip failure, V_{in} shorted to V_{out} and supplied both servos with an excessive 24 volts resulting in servo

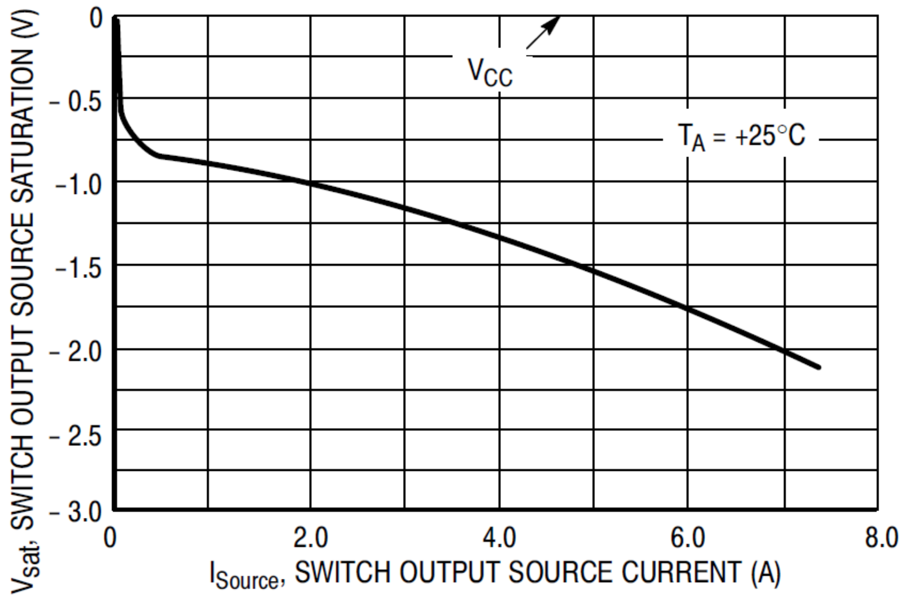

Figure 4.3: Switch output source saturation versus source current for the MC34167

failure. The shorting of the MC34167 is still an unknown mystery; however, provisions have been implemented to reduce the chance of servo failure in the event of a regulator short. To limit the voltage delivered to the servos, a transient voltage suppression (TVS) diode has been placed on the output of the regulator. Seen as D3 in Fig 4.2 this TVS diode clamps at just over 5 volts by shunting excess current, at approximately 6 volts the induced voltage exceeds the avalanche breakdown potential and the diode absorbs much of the transient energy. In the event that V_{out} approaches 6.0 volts for an extended period of time the fuse F1 will blow, protecting the circuit and the servos attached to it.

Servo position is dictated by a PWM signal from the microcontroller, which is produced from commands by the user from the dock, which are detailed in the wireless algorithm section. As presented in Table 4.1, pulse durations are specified to be at 50Hz and between 0.9 ms-2.1 ms with 1.5 ms as the center.

4.3 Sensors

SPI has been implemented with an array of sensors for both real-time control and post processing of their output data to quantify SPI's performance under predetermined circumstances and to gain understanding of specific events such as instabilities and high drag events. An Inertia Measuring Unit (IMU) and an Attitude and Heading Reference System (AHRS) has been installed in SPI with a single sensor array from CH Robotics known as the CHR-6dm AHRS. The CHR-6dm uses a 32-bit ARM Cortex processor to evaluate an Extended Kalman Filter (EKF) that combines data from onboard accelerometers, rate gyros, and magnetic sensors to produce yaw, pitch, and roll angle estimates. It is relayed to the system microcontroller over a Transistortransistor logic (TTL) 3.3V UART at 115200 Baud. In our implementation we have configured it to transmit raw sensor data in addition to Euler angle estimates for a packet that is formatted as [yaw, pitch, roll, yaw_rate, pitch_rate, roll_rate, mag_z, mag_y, mag_x, gyro_z, gyro_y, gyro_x, accel_z, accel_y, accel_x].

The 3.3V UART is not directly compatible with the system microcontroller; an AVR ATMEGA1284 expects a 5.0V UART. Communication between these two system requires a bi-directional level shifter; the MAX3372E from Maxim Integrated Products has been implemented to provide this functionality.

The CHR-6dm's sensor characteristics can been seen in Tables 4.2 and 4.3, which include their sensitivities [40]. In addition to acceleration measurements provided from the AHRS, a second more sensitive accelerometer has been installed in the longitudinal direction to achieve a higher accuracy of tail performance with the option to perform integration to obtain velocity data. This additional accelerometer, the MMA1260KEG from Freescale Semiconductor has a sensitivity of $1200mV/g$ which is 4 times higher than that of the CHR-

Table 4.2: Gyro Electrical Characteristics

Symbol	Parameter	Test Condition	Min.	Typ.	Max.	Unit
FSA	Measurement Range	4x OUT (amplified)		+/- 100		/s
FS	Measurement Range	OUT (not amplified)		+/- 400		/s
SoA	Sensitivity	4x OUT (amplified)		10		mV//s
So	Sensitivity	OUT (not amplified)		2.5		mV//s
SoDr	Sensitivity change vs temperature	Delta from 25 C		0.03		%//s
Voff	Zero-rate level			1.23		V
Vref	Reference voltage			1.23		V
OffDr	Zero-rate level change vs. temperature	Delta from 25 C		0.02		/s/C
NL	Non linearity	Best fit straight line		+/- 1		% FS
BW	Bandwidth			140		Hz
Rn	Rate noise density			0.017		/s/rt Hz

Table 4.3: Accelerometer Electrical Characteristics

Symbol	Parameter	Test Condition	Min.	Typ.	Max.	Unit
aFS	Measurement Range		+/- 3	+/- 3.6		g
SoXYZ	Sensitivity	Vdd = 3 V	270	300	330	mV/g
Stemp	SCDTT	Vs = 3 V		0.01		%/C
nXY	X,Y noise density			150		ug/rt Hz
nZ	Z noise density			300		ug/rt Hz
offXY	X,Y 0 g voltage	Vs = 3 V	1.35	1.5	1.65	V
offZ	Z 0 g voltage	Vs = 3 V	1.2	1.5	1.8	V
aNL	Non linearity			+- .03		% FS
aBW		With external filter		140		Hz

6dm accelerometers.

4.4 Microcontroller and Digital to Analog Converter

Atmel's AVR microcontroller series were investigated as a suitable platform for SPI and was found to be more than adequate for the required goals of the project. There are many benefits to the AVR platform compared to similar platforms such as the PIC. The open source nature of the AVR platform has not only made them extremely popular but has fueled an assortment of development tools of which the majority are free. The ability to write programming code in the C language and compile with the GNU Compiler Collection (GCC) reduced a significant amount of overhead and cost without reducing the performance of the product. Currently, SPI is running the ATMEGA1284 microcontroller for its assortment of features and its large 40 pin dual in-line package (DIP), which facilitates quick and easy prototype development. The ATMEGA1284 is a high-performance 8-bit Reduced Instruction Set Computing (RISC) microcontroller with 128 Kilo Bytes (KB) of flash memory with read-while-write capabilities. This microcontroller included all the requirements sought for the project, which included a 10-bit analog to digital converter (ADC), three timers, several pulse width modulation (PWM) channels, Serial Peripheral Interface Bus (SPIB), as well as two programmable serial universal asynchronous receiver/transmitters (USARTs) . This single microcontroller provides the majority of processing power for the entire platform and performs many tasks. Its responsibilities include receiving wireless messages over the first USART and decoding them in real time to provide pulse widths for the motor driver and pectoral fins, operating the 8-channel ADC at 100Hz to obtain data from various sensors, acquiring data over the second USART from the Attitude Heading Reference System/Inertial

Measuring Unit (AHRS/IMU), logging all relevant information to a Secure Digital (SD) card on the Serial Peripheral Interface Bus, as well as making decisions for semi autonomous behavior in the event of communications failure.

Data acquisition was implemented on SPI to increase the productivity of current experiments as well as future experiments by designing the system with enough bandwidth for significant expansion. Data are collected from various sources on the AVR and written to a Secure Digital (SD) Card for post processing via the Serial Peripheral Interface Bus (SPIB) in raw ASCII in 512 byte blocks. It was determined that implementing a file system on the microcontroller was unnecessary. A file system required significant processing overhead and considerable programming space only for the luxury of being able to easily mount the SD card using conventional file system techniques. Writing to the SD Card without a file system greatly improves logging performance despite the cost of imposing technical challenges when trying to extract data from the card. This can easily be accomplished by the following GNU/Linux commands. Data are first extracted from the SD Card block by block into a log file using the dd command:

```
dd if=/dev/mmcblk0 of=Data.log bs=512 count=10000
```

where /dev/mmcblk0 is the SD device and Data.log is the destination for the data. Zeros are then trimmed from the log file using the tr command

```
tr -d ''\000'' < Data.log > Data_Trimmed.log.
```

Those two commands yield a file that can be interpreted with software of the user's choice. It is important to note here that the SD Card can easily be cleared or formatted with the dd command as well by writing zeros to each block of the card.

```
dd if=/dev/zero of=/dev/mmcblk0 bs=512 count=20000
```

Data is acquired not only from the CHR-6dm AHRS over a USART on the AVR but from the AVR's Analog to Digital Converter (ADC). The Atmega1284's ADC has 8 channels with 10-bit resolution currently sampling the output from the longitudinal accelerometer at 100Hz; the remaining 7 channels are available for future use. The specifications for the Atmega1284's ADC are [11]

- 10-bit Resolution
- 0.5 LSB Integral Non-linearity
- ± 2 LSB Absolute Accuracy
- 13 μs - 260 μs Conversion Time
- Up to 15 kSPS at Maximum Resolution
- 8 Multiplexed Single Ended Input Channels
- Differential mode with selectable gain at 1x, 10x or 200x
- Optional Left adjustment for ADC Result Readout
- 0 - VCC ADC Input Voltage Range
- 2.7 - VCC Differential ADC Voltage Range
- Selectable 2.56V or 1.1V ADC Reference Voltage
- Free Running or Single Conversion Mode
- ADC Start Conversion by Auto Triggering on Interrupt Sources
- Interrupt on ADC Conversion Complete
- Sleep Mode Noise Canceler

4.5 Wireless Interface

Single direction wireless communication from the dock to SPI is accomplished with a 315 MHz link over the air. This one-way communication is based around Holy Stone Enterprise's MO-SAWR-A transmitter on the dock and their MO-RXLC-A receiver installed inside of

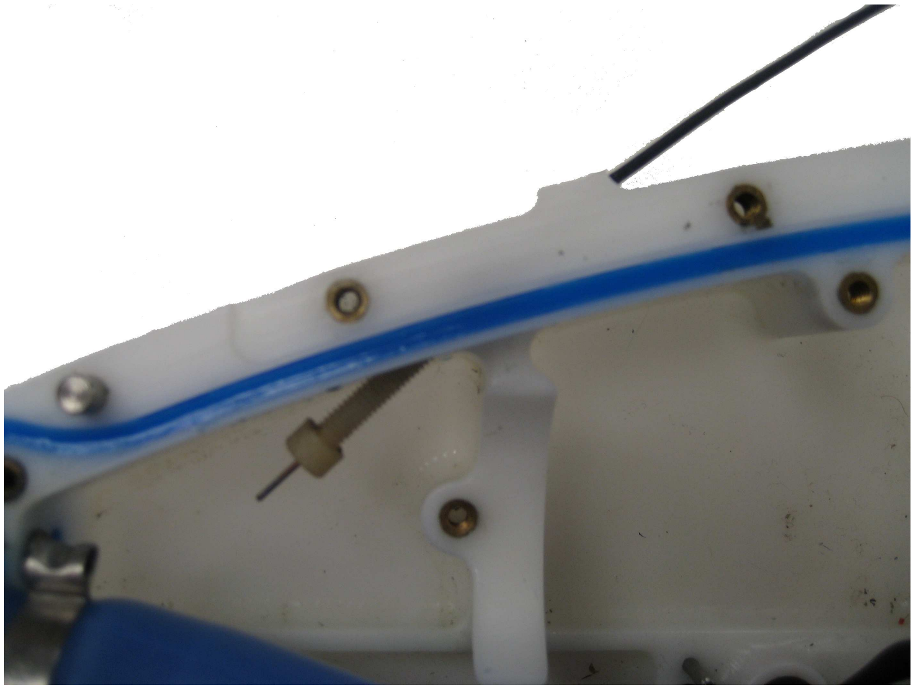

Figure 4.4: The SPI antenna which passes through the hull and extends 22.6 cm above the waterline.

SPI. Receiver installation inside the hull requires an antenna to pass through the hall and extend past the surface of the water to receive the wireless signal over-the-air. This was implemented by passing the 1/16" diameter antenna through the hull and sealing it with an o-ring under heavy compression provided by a custom designed sealing fastener that has provided a robust solution without the need for a sealant. The antenna, protected with Raychem heat shrink wrap as seen in Fig. 4.4, is a 1/4 wavelength antenna that measures 22.6 cm out of the water.

Initial bench top implementation of this communications package was very promising with distances over 100 feet and a fairly high baud rate of 2400bps, both of which were more than sufficient for the requirements of the wireless link. However, when installed inside the hull, significant noise from the pump and other circuitry completely disabled communications. After inspecting the circuitry and software, a solution of both hardware and software was implemented to restore the wireless link. The hardware modifications included isolating the receiver behind an LC (Inductor-Capacitor) circuit on both the power and ground side as well as implementing a high pass filter on the antenna itself. Increased encoding was implemented in the software which, with the combination of the hardware modifications restored wireless communications with a slightly lower throughput from the additional overhead of the checksums for the data packets. Details of the wireless algorithm can be found in chapter 5.

4.6 Power Supply

SPI's monocoque hull was designed to accommodate 20 AA batteries with room to spare for additional, unanticipated components. The AA battery size was chosen for its availability and ease of creating custom battery packs. AA batteries are plentiful in a variety of different chemistries and are relatively inexpensive compared to new battery technologies such as lithium polymers. SPI's current battery chemistry is Nickel-Metal Hydride (NiMh), it was primarily chosen for its high ampere-hour rating and its density. Battery placement in the hull has been designed to be as low as possible; the high density of NiMh batteries is beneficial for the CG location. Another important feature of NiMh batteries is their ability to be charged with relative ease and safety compared to lithium based battery technologies.

SPI's current batteries are Panasonic's HHR-210AAC4B with a minimum rating of 2000mAh with a nominal voltage of 1.2V. These 20 AA batteries are installed in series for a nominal battery pack voltage of 24V. The batteries are assembled into 4 packs of 5 batteries each and are enclosed in chemical resistant heat shrink wrap from Raychem to contain the possibility of explosion as seen in Fig.4.5. In addition to providing safety from

Figure 4.5: An exploded NiMh cell as a result of a short in the system can be seen here. The chemical resistant heat shrink completely contained the failure protecting, SPI, the environment and personnel.

battery explosions, the Raychem shrink wrap provides an ultra durable protective coat that not only protects the batteries from mishandling and abrasions but completely water proofs them so that in the event of hull failure the in-line fuse will have the opportunity to blow and completely isolate the battery system avoiding the possibility of contaminating the environment.

The batteries were chosen to be installed in series for the ability to drive the pump at higher voltages for increased flow for short periods of time it is found necessary. An added benefit from having the batteries in series is the simplified charging circuit as well as the safety associated with the battery pack. SPI has been designed to enable charging through the charging port rather than opening the entire hull, which greatly reduces the time and effort to charge SPI.

Chapter 5

Software

5.1 Introduction

The SPI project has included several software programs to provide the platform with an assortment of tools and features to streamline testing procedures and get the full benefit of the data acquisition system. In general, there are two primary programs that are required to facilitate a testing session: software running on the AVR microcontroller inside SPI as well as supporting software running on a laptop computer on the shore, or dock. In addition to these two primary programs, software has been written to post process sensor data including filtering and plotting capabilities.

Communications between the user and SPI are outlined in Fig. 5.1, which shows an overview of the communications including the various protocols and media that are used between devices. The wireless algorithm used for encoding and decoding the wireless signal as outlined in the figure is included in this chapter. In addition to providing a communications link between the user and SPI the programs running on both the laptop and on SPI perform

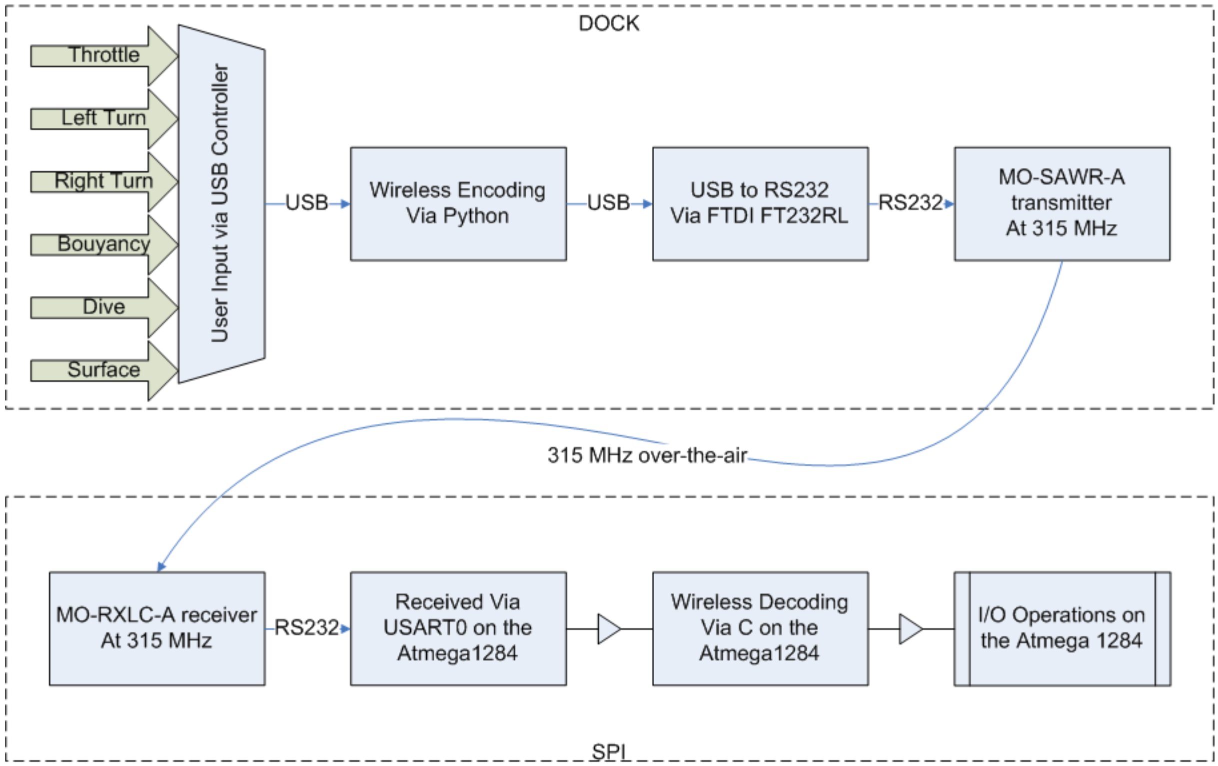

Figure 5.1: A high level flow chart that lays out the flow of communications from the user to SPI including the communications protocols and media that are used.

many other tasks that are outlined in the following sections.

5.2 Client Software

Client software written in Python, is currently executed on an IBM Thinkpad running Debian Linux and is responsible for capturing the user inputs through a game controller, assembling the requests in a predefined manner and broadcasting the user requests over the wireless link. User commands are interpreted from their inputs on a Logitec *Dual Action* USB controller plugged into the laptop. The user has two analog joy sticks, two triggers, and an array of buttons that are custom programed to perform a variety of tasks. The analog joy sticks are primarily used for turning and diving commands while the triggers are used for the throttle.

The various buttons on the controller have been programmed to perform predefined sets of instructions, such as issuing ramp inputs to the throttle or turning sequences. These user commands are recorded to a local timestamped log file as well as supplying the user with useful outputs to the terminal such as the throttle ON/OFF events.

The ability to program a previously determined set of instructions ensures that a given test can be executed multiple times without concern that the user's inputs have changed. Significant work has been put forth to minimize the amount of time SPI needs to be removed from testing to perform software maintenance; soft limits and calibration are present in the client software that give comlpete control to the user without the need to open SPI in order to reprogramming the microcontroller. This is beneficial for two reasons: first, reducing the programing overhead to adjust parameters saves significant time during testing sessions by adding flexibility to testing procedures, and, modifying parameters and configuration changes in Python is significantly easier and faster than performing the same task on the microcontroller, which is written in C with very specific requirements to remain compatible with the AVR microcontroller.

5.3 Wireless Encoding and Decoding

As mentioned in the Wireless Interface section noise in the electronics, primary from the pump degraded the performance of the wireless link to a state that was no longer sufficient for transmitting data. The excess noise picked up by both the antenna and the receiver circuity overwhelmed the USART buffer resulting in the polluting of the data packets with garbage. After designing and implementing analog hardware filters it was also required to provide an encoding and decoding algorithm for the wireless signal to ensure that only valid packets were processed by the microcontroller. Manchester style encoding was first evaluated but was found not to be sufficient for the desired data packet and the environment to which it was exposed. Manchester encoding operates on the bit level; for simplicity of packet transmission and programming in both SPI and in the client software it was desired to directly send American Standard Code for Information Interchange (ASCII), which operates on top of the bit level. It was found that including a simple checksum to each command resulted in an acceptable and sufficient transmission of desired commands.

Currently, SPI operates on three independent commands that are sent to it from the user: throttle, left pectoral position, and right pectoral potion. Each of these commands has been compressed from its initial values of $000-255$ to $000-099$ to accommodate the packet size and algorithm. For example, the throttle command has been allocated numbers between $000-099$ with check sum values between $100-199$. The algorithm is fairly straight forward: consider a desired throttle value of 050, the client software first sends that value, then adds 100 to the desired value and send the second value of 150. SPI receives the first message, because the value is between 000 and 099 it is assumed that this is a throttle command. If the next message SPI receives is 150, SPI then processes the command as valid and applies the desired throttle position. To maintain a high throughput it has been decided that all commands will be 3 digits in length resulting in 500 unique commands between 000 and 999 which include their checksum values. These allocations have been outlined in table 5.1 with the addition of reserved space for future commands.

The wireless system runs at a baud of 2400bps and has the ability to adjust its gain on the receiver side to help increase distance. While this can be quite beneficial, it requires a continuous stream of data to be received for the gain to maintain an acceptable value. In

Table 5.1: Encoding and checksum values for the wireless algorithm.

Command Name	Command	Checksum	Checksum Value
Throttle	0-99	100	100-199
Left Hydroplane	200-299	100	300-399
Right Hydroplane	400-499	100	500-599
Left Turn	600-649	50	650-699
Right Turn	700-749	50	750-799
Depth	800-849	50	850-899
Forward CG Buoyancy	900	1	901
Rearward CG Buoyancy	902	1	903
Dive Buoyancy	904	1	905
Surface Buoyancy	906	1	907

the event that there is a pause in the data, gain in the receiver increases and a considerable amount of garbage is send into the USART RX buffer when underlying noise is amplified. As the buffer becomes overwhelmed from the increased noise, the actual data messages get lost in the translation and it become erroneous. In addition to the wireless algorithm, zero padding has been included in the header of each packet to help set the gain in the receiver before critical data are received.

5.4 Microcontroller Software

Software that resides on the Atmega1284 has been written in the C programming language and compiled with AVR-GCC. The software is quite complex and includes many features that are specific to the family of AVR microcontrollers. This software is the heart of SPI and is responsible for all of the Input/Output (I/O) operations that happen during standard operation. In addition to providing and maintaining I/O operations this code has been implemented with autonomous operations to surface the platform in the event the communications have been lost for a duration of 10 seconds.

Hardware interrupts have been implemented in the software to guarantee log rates and to ensure that all packets received over the USART are accounted for. Log rates are guaranteed with the use of a timer and an interrupt. A timer is analogous to a simple counter; however, its advantage is that it is independent of program execution and relies only on the input clock of the microcontroller, which results in a very stable frequency. Hardware interrupts are issued when the programed timer reaches a designated value. At that instant the required logging sequence is initiated and data are logged are a consistent rate for the duration of experiment. When packets are received into one of the USART buffers, either from the wireless transmitter or the AHRS, a hardware interrupt is issued and the packet is processed immediately, clearing the USART buffer for future packets.

There are several timers on the Atmega1284 that are used for guaranteeing log rates as well as controlling PWM outputs. Using a timer to control a PWM output removes the need manually apply a modulated signal to an output pin of the microcontroller. By associating a PWM output pin with a hardware timer the PWM signal is generated automatically, without the need to for software intervention. In addition to these advanced features of AVR microcontrollers, it is important to note that they are not limited to 8 bit math, using the AVR-GCC compiler, these microcontrollers can easily perform floating point math and even handle 64 bit numbers. These features of the microcontroller reduce programming time and effort and result in readable and efficient code that is not restricted by their 8 bit core.

Chapter 6

Experimental Methods

6.1 Introduction

Quantifying the performance of fluttering tails has proven to be time consuming as well as challenging. Testing a submersible adds significant complications that are not present with platforms that exist outside of water. Not only does the waterproofing of the platform require significant design work and maintenance, testing sessions have an extended duration while waiting for pool currents to reside and conditions to be acceptable for testing. The testing conditions SPI is exposed to have helped develop the primary goals of the platform. These goals were set forth to minimize the down time during testing by designing a robust platform that could sustain the forces exposed to it from the testing environment and to ensure that maintenance and routine changes were straightforward and required minimal tools and knowledge of the platform.

Numerous experiments have been conducted to characterize and test SPI for durability and longevity as a whole, including that the hull is water tight, wireless algorithms are sufficient, data acquisition is in working order, and that SPI is robust enough handle unforeseen circumstances such as collisions and extreme depths. It is crucial that the platform performs as expected and carries out its required tasks such that testing sessions are dedicated to quantifying the performance of fluttering tails rather than debugging the experimental platform. Initial testing of the hull was performed in a 50 gallon fish tank where it was submerged for a total of 24 hours. This test proved that the hull was indeed a water tight enclosure and it was then populated with electronics and the actual testing of the platform began. It was proven to be a feasible platform in several tests in the diving well at Michigan State University's Intramural West Facility including an extended swim for the duration of several minutes at a depth of 17 feet in the bottom of the diving well during which SPI collided with the walls at approximately $1m/s$. The results of this particular test (which was not intended to happen) proved that SPI was sufficiently durable and that semi-autonomous behavior to return to the surface was needed when communications were lost.

Since the initial validation of the experimental platform, significant time has been spent characterizing both tail and hydroplane performance. Fluttering tail performance has been compared to a rigid tail as well as a rigid tube to quantify its performance and efficiency, these tails can be seen in Fig.6.1 . The rigid tail is geometrically similar to that of the fluttering tail, it maintains the same aspect ratio, area, and density; it only differs from the fluttering tail by its thickness and material choice which make it sufficiently stiff. The rigid tube maintains the same cross sectional area of the fluid-conveying pipe as the flexible and rigid tails and is designed such that the exit conditions of the jet are the same as the flexible and rigid tails.

Open water testing has been performed exclusively in the indoor diving well at Michigan

Figure 6.1: Three different tail geometries have been testing with the experimental platform. (Top) A rigid tail with identical geometry and buoyancy of a flexible tail. (Middle) A rigid tube that has the same length and fluid jet exit conditions as a corresponding rigid of flexible tail. (Bottom) The flexible tail, made of neutrally buoyant latex a constructed using the butt-welded method.

State University's Intramural West Facility. The diving well is approximately 2500 square feet on the surface and is sufficiently deep for our current needs. At this time of writing SPI has been in service for a total of 5 months and has swam in the diving well for a total of 21.0 hours, 20.7 of those hours have been logged as time when the pump has been on. There have only been two notable incidents during these test events, both incidents were of human error, which resulted in a collection of moisture in the access port on the left side of SPI as a result of not applying enough torque to the sealing fastener. In both cases, the leak was unnoticed during the testing session and was only discovered when the access port was opened to turn off the electronics.

6.2 Free Locomotion

Initial testing of the SPI was completely untethered. We began by giving SPI a throttle command and then studied the stability and robustness of the platform. In regards to the stability of SPI we focused on its behaviors in roll, pitch, and yaw, as well as its ability track a straight line trajectory. Using our observations we made small adjustments to the location of the center of gravity with respect to the center of buoyancy to improve stability in roll, pitch, and yaw. Straight line tracking was improved with the addition of control surfaces including keels and rudders with the latter greatly improving the straight line tracking ability.

It is important to note here that SPI was not designed to swim in a straight line, it was designed to be quick and agile and accepting of a control strategy that would provide the means necessary to track trajectory. Furthermore, it was designed to investigate the possibility of induced turning events by modulating the flow rate of the fluid conveying pipe. The control strategy is a topic of future research and important steps need to be taken to support these future goals. First and foremost, quantifying the performance of fluttering tails is the first step to continuing this research. Our motivation behind improving SPI's straight line tracking ability was to minimize the error when collecting data to quantify tail performance.

Even though SPI was designed with quickness and agility in mind, its modular design has allowed it to accommodate a selection of fins to modify its behavior in order to provide satisfactory tracking performance. The flexibility of this platform has proven extremely beneficial. Fin and rudder changes can be performed pool side with a single tool without the need to visit a machine shop or carry an entire box of tools.

Unfortunately, currents in the Intramural swimming pool have proven to be considerably strong. Their effects on SPI's straight line trajectory have been so severe that we have opted to design a guide-string system to maintain a relatively straight path to minimize erroneous data.

6.3 Guided Locomotion

As previously mentioned, experimental testing with the guide-string system was implemented to reduce erroneous data and increase the efficiency of our test sessions. However, the tethering of SPI with a guide string is not to be confused with tethering systems that incorporate data and power to mobile robots. Our guide-string system has a single purpose which is to provide straight line tracking for SPI. It does not provide SPI with power or communications, SPI is still operated over the 315MHz wireless link and provides its own source for power with its 20 NiMh AA batteries. Guided locomotion has been achieved over a 50 foot span in the diving well by implementing a taunt nylon guide string over the distance. SPI has an attachment that mounts to its dorsal fin to accommodate the guide string, which can be seen in Fig 6.2. The guide string forces SPI to maintain a straight trajectory so a valid comparison between the performance of various tails can easily be achieved.

To quickly and efficiently test SPI on a guide string, a custom tram has been developed as seen in Fig 6.2. The tram has an internally polished stainless steel tube that provides guidance that is connected to the dorsal fin with a rotary locking mechanism that allows SPI to be quickly turned around on the tram without removing it from the guide string. The rotary locking mechanism is equipped with two detents to lock SPIs position in either 0 or 180 degrees ensuring proper alignment. The stainless steel tube only provides a suggested guidance for SPI. SPI is still free to roll about the string as well as pitch forward and rearward at the location of the dorsal fin/tram junction. This combination of constraints allows SPI to operate with a minimum amount of influence from the guide string, ensuring that stability and control of the platform is still a requirement.

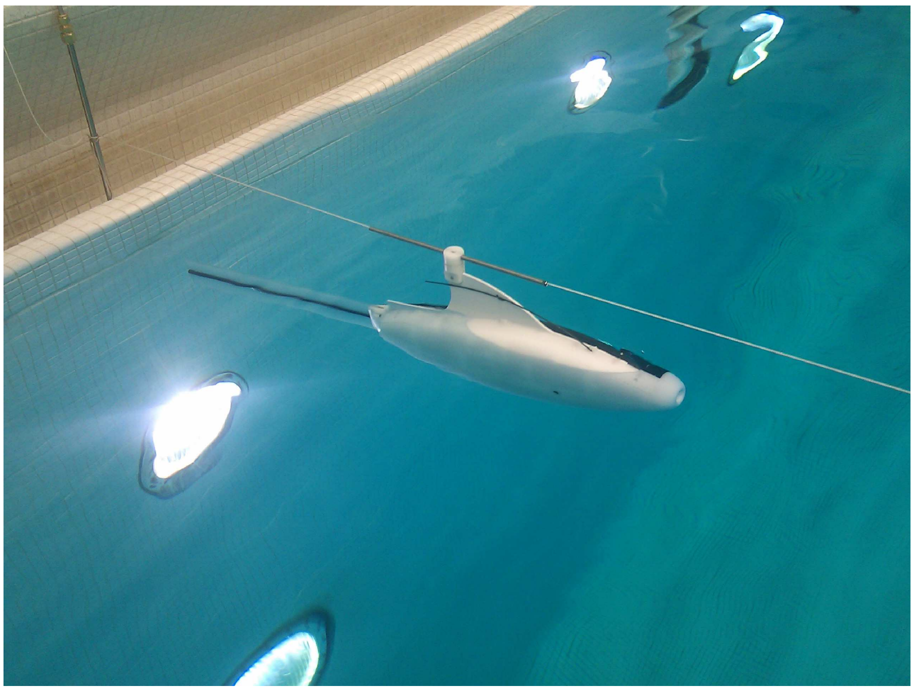

Figure 6.2: SPI testing under guide string conditions with a rigid tail. The guide strings only purpose is to provide a straight trajectory for SPI; power and communications are identical between free and guided locomotion.

Chapter 7

Experimental Results

As mentioned in Experimental Methods, to quantify the performance of SPI, its speed was determined using both flexible tails and a rigid tail of identical dimensions and buoyancy. In addition to these tails, a rigid tube of equal length and internal diameter affixed in place of the tails has also been included. Measurements conducted with the rigid tube represent a baseline performance which a viable implementation that SPI must exceed. The presence of the tube, as opposed to simply removing all attachments from the tail barb, was required in order to stabilize the vehicle; it was found that removing the tube led to a pitch instability of the hull. Figure 7.1 is a sequence of images taken over 1 sec. of operation; these images were acquired while SPI was accelerating from rest, during which time we could take pictures more normal to the free surface to reduce glare. The reduced forward speed during acceleration also leads to a longer period of oscillation of the tail; Fig 7.1 indicates a period of 0.8 seconds, compared to a period of 0.33 seconds observed when SPI is at top speed.

The average speed of SPI has been measured by analyzing 30 frame/second video taken during operation; the guide string has been marked at two locations 9.14m apart, and the

Figure 7.1: High-speed images of the SPI acquired over a period of 1 sec, soon after it started from rest in the MSU swimming pool. The SPI was moving with an average speed of ≈ 0.4BL/s, less than the maximum speed of ≈1.15BL/s; note the large deflections of the tail which occur during acceleration.

Table 7.1: Mean speeds of the three tested configurations in meters and body lengths per second for all runs performed to date.

Configuration	Trails	Speed [m/s](N)	Speed [BL/s](N)	Speed [m/s](S)	Speed [BL/s](S)
Rigid Tube	42	0.725	0.929	0.795	1.019
Rigid Tail	45	0.759	0.973	0.814	1.044
Flexible Tail	88	0.648	0.831	0.707	0.906

times at which the SPI crosses these marks can be determined, and the speed calculated. To date we have performed 175 runs over the 50' span in the swimming pool, the calculated speeds are given in Table 7.1 as well as in Fig.7.2 which includes error bars denoting the limits of 95% confidence intervals. The majority of these tests have been performed near the surface of the pool to maintain a wireless connection. Through iterations of our testing we have learned that the loss of energy due to free surface effects has a substantial influence on the speed of the platform.

To limit loss of energy due to free surface effects, the mass and center of mass of SPI were adjusted such that the measured portion of the run was entirely below the surface. The results of these runs can be seen in Table 7.2 as well as in Fig.7.3 which includes error bars.

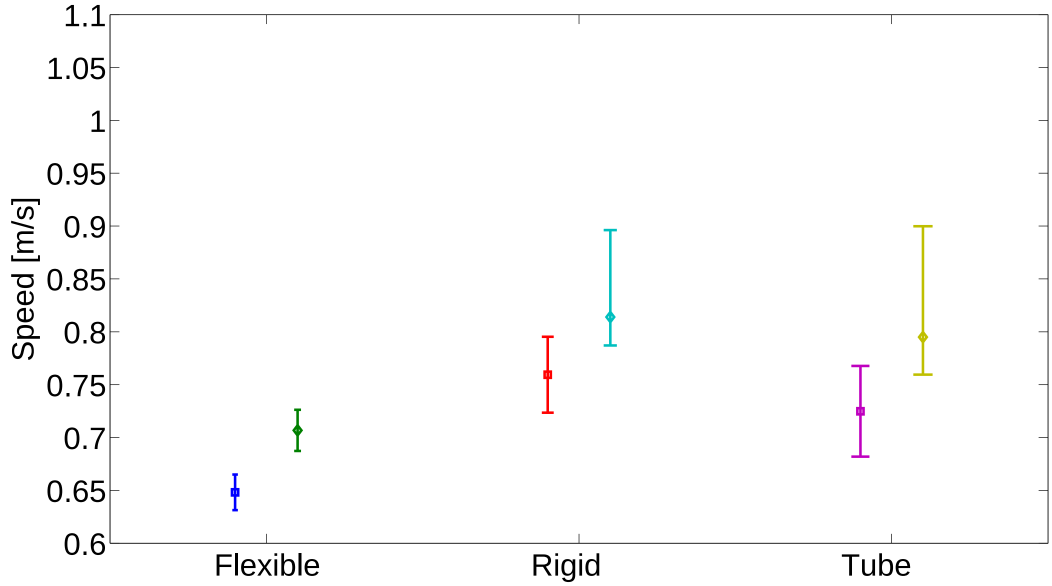

Figure 7.2: Average speeds of the configurations listed in Table 7.1 which include 175 runs, with error bars denoting the limits of the 95% confidence intervals. Points denoted by a □ indicate runs which traveled North in direction while points denoted with a ◊ indicate runs in the opposite direction.

Table 7.2: Mean speeds of the three tested configurations in meters and body lengths per second for all submerged runs.

Configuration	Trails	Speed [m/s](N)	Speed [BL/s](N)	Speed [m/s](S)	Speed [BL/s](S)
Rigid Tube	14	0.806	1.033	0.872	1.118
Rigid Tail	32	0.794	1.018	0.845	1.083
Flexible Tail	14	0.744	0.954	0.811	1.040

The difference between these selected runs is significant and shows that the performance of the flutter tail is on par with the both the rigid tail and the rigid tube. We believe that future improvements in tail design which are currently being pursued will allow the rigid tube baseline to be surpassed.

As seen in Figs.7.2 and 7.3 there is a significant difference between runs which travel in the North direction compared to ones which travel in the South direction. This difference has been contributed to the various currents that are present in the pool. These pool currents are

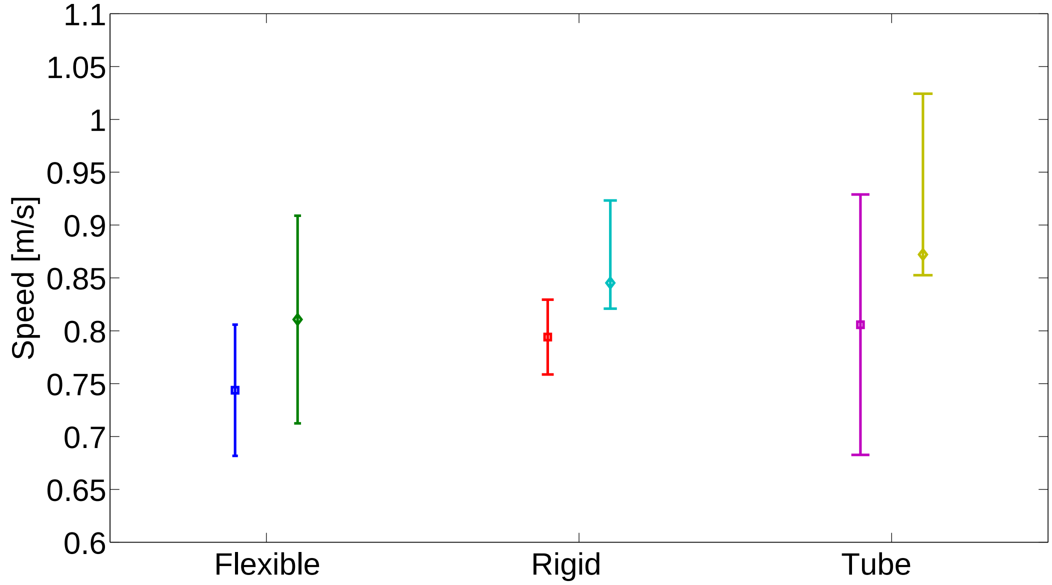

Figure 7.3: Average speeds of the configurations listed in Table 7.2 which were performed completely under the surface of the water totaling 60 runs. Error bars denoting the limits of the 95% confidence intervals, points denoted by a □ indicate runs which traveled North in direction while points denoted with a ◊ indicate runs in the opposite direction.

artifacts of the circulation and filtration system as well as the disruptions from lap swimmers and occasional divers. It will be desirable in future test sessions to perform our testing in the absence of the circulation and filtration system as well as the pools patrons.

Chapter 8

Future Improvements

Although SPI has proven to be a successful and robust platform we believe we can increase our productivity by improving a few designs and adding additional features to the platform. There are several features, which will be detailed in this chapter, that are currently in the design stages that have not been completed at the time of this writing. In addition to these new features, there are some improvements that can be made to the platform to increase its ease of use.

To fully quantify the performance of the platform, it is desirable to know the characteristics of the prime mover. We have proposed to include a calibrated elbow inside the hull as seen in Fig.8.1, which connects the exit of the pump to the nozzle of the platform in two $90°$ opposing bends. The addition to this calibrated elbow, we will require a single differential pressure sensor as well as a means for measuring the voltage and current delivered to the prime mover. After performing a bench-top calibration of the flow system we will have a characteristic curve of our prime mover for the range in which it operates. The characteristic curve will provide the means necessary to have the ability to close the loop for flow control,

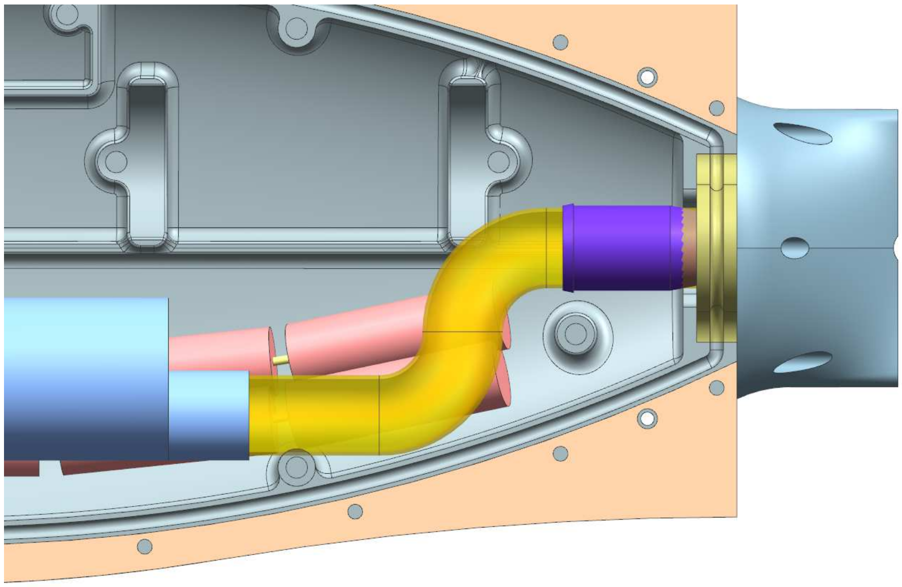

Figure 8.1: The proposed calibrated elbow that will provide SPI with the means necessary to provide a consistent flow rate to the tail regardless of the state of the power supply.

enabling us to provide consistent flow rates regardless of the state of the power supply.

As the circuit designs have approached their final iterations we have started to lay out a final Printed Circuit Board (PCB) design to shrink the current package from its axially installed components to smaller surface mount devices. The move to surface mount devices will decrease the size and complexity of the circuits providing more real estate inside the hull in addition to providing us with a quick method to produce multiple circuit boards. Current plans are to include a surface mount pressure sensor for the calibrated elbow as well as the required current and voltage sensors for the prime mover. The PCB will also include the necessary components to control ballast tanks that are currently in the design process as well.

We have found a single drawback with SPI's current design, the method in which the tail is *clamped* to the hull has proved to be somewhat time consuming and slightly disruptive to our tails when removing them from the tail clamping component. Although the current solution is acceptable and works in the manner envisioned, removal of the tail is not as easy and forgiving as it should be and has caused de-lamination on some of our tail specimens. With slight modifications to the current tail clamp, we will be able to overcome its current limitations and provide a solution to quickly change tails without fear of possible de-lamination.

At some point in the future it will be desirable to develop a tail manufacturing process that will enable us to manufacture tails that are not restricted to 2D shapes as they currently are by our laminating and butt adhering methods. The ability to construct tails that vary in cross sectional widths and heights will be beneficial as we push the envelope in the design of fluttering tails. Tail shapes that are similar to fish may be feasible by developing casting compounds that are neutrally buoyant and creating 3D molds that represent desirable shapes.

The most anticipated improvement to the SPI platform is providing a solution for underwater communications. This has proven not to be a trivial task with solutions such as the WHOI micro-modem exceeding the cost of SPI by a significant margin. To add to the complications, it is not guaranteed that the WHOI micro-modem will even package inside of SPI. These constraints have restricted us to perform our experiments at the surface of the water where we can maintain over-the-air wireless communications.

Chapter 9

Conclusions and Future Research

We have successfully developed an underwater experimental platform for studying the behavior and performance of a submersible propelled by a fluid-conveying fluttering tail. We have proved its robustness with over 20 hours of pool testing without a single substantial breech in the hull. Not only have we designed a robust and dependable platform, we have designed it to be as modular as possible to accommodate a variety of prime movers and fin assortments, which include both active and passive arrangements. We have included unique features in the design that have streamlined testing procedures and provided a platform that will sustain further research and development by enabling adjustments and modifications without the need for a complete redesign of the major hull, reducing design time and complexity. We have included a data acquisition system running at 100 Hz to obtain data from an Attitude Heading Reference System/Inertial Measuring Unit (AHRS/IMU) along with an 8 channel 10 bit Analog to Digital Converter to provide the tools necessary to completely understand the dynamics of the platform. We've designed the electronics system including the circuitry, computing platform, actuators, and drivers to be as simple as possible without reducing SPI's performance or limiting its potential. It has been designed built using off-the-shelf components that are easily and inexpensively replaced in the event of a breech in the hull.

SPI has already proven its effectiveness by producing a candidate for the *IEEE/ASME Transactions on Mechatronics* journal [42] as well as two conference papers: one for *2011 Dynamic Systems and Control Conference* [43] and another for the *IEEE/RSJ International Conference on Intelligent Robots and Systems* [44]. These initial papers are based on the investigation of straight line performance of fluttering tails, which represents the beginning of our research into this topic. It has been proposed that further research on the topic of fluid-conveying fluttering tails is to investigate the possibility of induced turning by modulating the flow and pressure through the fluid conveying tail. In addition to this investigation it will be necessary to add additional supporting features to the platform including depth and stability control. These additional features will help minimize the losses and effects of the wake and to maintain a stable platform that is acceptable to our control inputs.

APPENDICIES

Appendix A

Dynamic Model Literature Review

A.1 Uniform Velocity Profile

The earliest work pertinent to the study of dynamics of fluid-conveying flexible pipes can be traced back to a series of experiments by John Aitken F.R.S.E. in the *Philosophical Magazine and Journal of Science* in 1878. Aitken, (a Scottish meteorologist, physicist, and engineer) stated that these experiments did not contain much that was new but helped to fill an evident gap in the experimental dynamics and hoped that they would enable the general reader to form a clearer idea of the action of the so-called centrifugal force [1]. The phenomenon of spontaneous motions from the free end of a flexible hose was first recognized as a self-excited oscillation by the French physicist and mathematician Louis Marcel Brillouin in 1885; however, his work was never published and existed only as *dans une Note de laboratoire* or laboratory notes. Bourrières, a student of Brillouin embarked on the study of the oscillatory instability of cantilevered fluid-conveying pipes, which was published in 1939 including both theoretical and experimental results [7] that included the correct equation of motion and experimental results outlining the critical flow velocity for the onset of oscillation.

Vibration in fluid-conveying pipes was revisited in 1950 in connection with the study of the Trans-Arabian pipeline vibrations between simply supported ends by Ashley and Haviland [2]. Feodosev [12] and Housner [27] studied the problem independently and came to the conclusion that for sufficiently high flow velocities, pipes may buckle in a similar manner to column buckling from sufficiently high compressive loads in the axial direction. Using a more general approach, Niordson [33] obtained the same equation of motion and the same conclusions of buckling and stability as Feodosev and Housner. In 1955, Long [29] revisited, among other boundary conditions, the dynamics of cantilevered fluid-conveying pipes previously studied by Bourrières to obtain methods of solution for relatively low fluid velocities which were below the critical threshold of the self-excited oscillation. He successfully perceived and experimentally verified that forced motions of cantilevered fluid-conveying pipes were dampened by the internal flow in the pipe for all flow vibrations he considered.

Oscillatory instability or flutter was anticipated by Benjamin [5, 6] in 1961, when he considering the dynamics of articulated pipes conveying fluid. Benjamin noted that the dynamics of cantilevered fluid-conveying pipes were independent of the fluid friction and analytically predicted the existence of flutter instability. In 1966 Gregory and Païdoussis [17, 18] predicted theoretically and proved experimentally that at sufficiently high flow velocities cantilevered pipes were subject to flutter rather than buckling. Benjamin found that buckling instability was present in vertical cantilevered articulated pipes, Païdoussis found that a continuously flexible pipe subject to the same scenario would never be subject to buckling [34], which was clarified in 1970 by Païdoussis and Diksnis [36].

Significant research was performed in the 1960s through 1980s extending the analysis

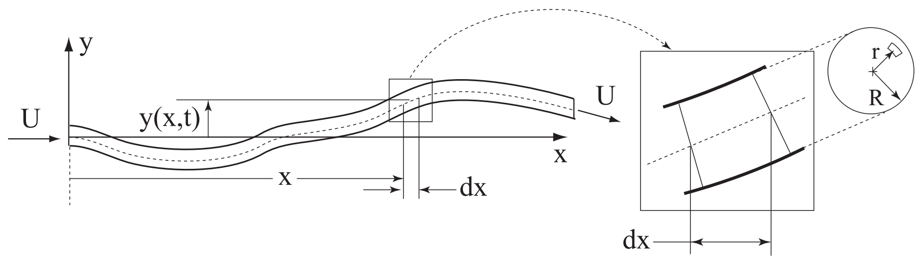

Figure A.1: A fluid-conveying pipe and a magnified view of a small element along its length including the cross sectional dimensions.

of cantilevered fluid-conveying pipes to include stability analysis by Nemat-Nasser, Prasad, and Herrmann [31, 24, 25], Timoshenko beam models by Païdoussis and Laither [38], non-linear formulations by Baja et al., Holmes, and Lundgren et al. [3, 26, 30], external flows by Hannoyer and Païdoussis [19] as well as unsteady flows by Païdoussis and Issid [37] of which details the analysis of uniform velocity profiles in flexible pipes.

Consider the fluid element in Fig.A.2 of length dx with an enclosed volume of $\delta\mathcal{V}$, which is a section of the fluid-conveying pipe in Fig.A.1. Assume that fluttering motions of the pipe are constrained to a single plane and that motions in this plane are relatively small in comparison to the length of the pipe. The rate of change of momentum over the fluid volume $\delta\mathcal{V}$ can be expressed as

$$\frac{\mathrm{d}\mathcal{M}}{\mathrm{d}t} = \int\int\int_{\delta\mathcal{V}} \left[\frac{\partial V_f}{\partial t} + (V_f \cdot \nabla)V_f\right]\rho \mathrm{d}\mathcal{V} \tag{A.1}$$

where d$\mathcal{V}$ is a small element found within the fluid volume $\partial\mathcal{V}$ and V_f is an approximation of the fluid velocity inside the pipe. Assume that the fluid inside the pipe travels through the pipe as a single infinitely flexible rod at the same velocity U relative to the pipe itself at all points. This approximation is known as plug flow and is a reasonable approximation for a fully developed turbulent flow profile. Ignoring secondary flow effects as well as radial variations [37], the velocity of the pipe itself, V_p can be expressed as

$$V_p = \frac{\partial \mathbf{r}}{\partial t} = \dot{x}\mathbf{i} + \dot{y}\mathbf{j} \tag{A.2}$$

where $\mathbf{r}$ is the position vector from the origin to an arbitrary point along the fluid-conveying pipe in Fig.A.1. $\dot{x}$ and $\dot{y}$ are the velocities of a particular point in the x and y directions respectively. The velocity, V_f of the center point of the fluid element in Fig.A.2 can be expressed as a function of the velocity, V_p of the pipe as well as the fluid velocity U relative to the pipe

$$V_f = V_p + U\boldsymbol{\tau} \tag{A.3}$$

where $\boldsymbol{\tau}$ is the unit vector tangent to the pipe at the point of interest

$$\boldsymbol{\tau} = \frac{\partial x}{\partial s}\mathbf{i} + \frac{\partial y}{\partial s}\mathbf{j} \tag{A.4}$$

where s is the curvilinear coordinate along the length of the pipe. Expanding Eq.(A.3) and collecting terms

$$V_f = \left(\dot{x} + U\frac{\partial x}{\partial s}\right)\mathbf{i} + \left(\dot{y} + U\frac{\partial y}{\partial s}\right)\mathbf{j}. \tag{A.5}$$

V_f in the above equation is known as the material derivative, $\mathrm{D}\mathbf{r}/\mathrm{D}t$, for the fluid element in Fig.A.2. Eq.(A.5) can be reduced further based on previous assumptions; relatively small oscillations suggests that $\partial(dx/ds) \simeq 1$ as well as $\partial(dx/dt) \sim \mathcal{O}(\epsilon^2)$. These assumptions yield the fluid velocity as found in Païdoussis' *Fluid-Structure Interactions* [35]

$$V_f = U\mathbf{i} + \left[\frac{\partial y}{\partial t} + U\frac{\partial y}{\partial s}\right]\mathbf{j} \tag{A.6}$$

Taking the derivative of V_f in Eq.(A.6) with respect to time to obtain the first term found in the integrand of Eq.(A.1) yields

$$\frac{\partial V_f}{\partial t} = \frac{\mathrm{d}U}{\mathrm{d}t}\mathbf{i} + \left(\frac{\partial^2 y}{\partial t^2} + U\frac{\partial^2 y}{\partial s \partial t} + \frac{\mathrm{d}U}{\mathrm{d}t}\frac{\partial y}{\partial s}\right)\mathbf{j}. \tag{A.7}$$

The second term in the integrand, $(V_f \cdot \nabla)V_f$, known as the convective operator, is evaluated as follows:

$$(V_f \cdot \nabla)V_f = \left(V_s\frac{\partial V_s}{\partial s} + \cancelto{0}{V_y\frac{\partial V_s}{\partial y}}\right)\mathbf{i} + \left(V_s\frac{\partial V_y}{\partial s} + \cancelto{0}{V_y\frac{\partial V_y}{\partial y}}\right)\mathbf{j} \tag{A.8}$$

where $V_y \partial V_s/\partial y$ and $V_y \partial V_y/\partial y$ are exactly zero. Evaluating the remaining partial derivatives and recalling that $\partial(dx/ds) \simeq 1$ yields

$$(V_f \cdot \nabla)V_f = U\frac{\partial}{\partial x}\left[U\mathbf{i} + \left(\frac{\partial y}{\partial t} + U\frac{\partial y}{\partial s}\right)\mathbf{j}\right] = \left(U\frac{\partial^2 y}{\partial x \partial t} + U^2\frac{\partial^2 y}{\partial x^2}\right)\mathbf{j}. \tag{A.9}$$

Combining Eq.(A.7) and Eq.(A.9) yields the rate of change of momentum with respect to the free-body diagram found in Fig.A.2, which is

$$\frac{\mathrm{d}\mathcal{M}}{\mathrm{d}t} = M\frac{\mathrm{d}U}{\mathrm{d}t}\delta s\,\mathbf{i} + M\left[\frac{\partial^2}{\partial t^2} + 2U\frac{\partial^2}{\partial t \partial x} + U^2\frac{\partial^2}{\partial x^2}\right]y\delta s\,\mathbf{j}. \tag{A.10}$$

To obtain an equation of motion for the fluid-conveying pipe, the equations of motion for the fluid element and the corresponding fluid-conveying pipe element need to be determined. Once determined and combined with the momentum over the fluid volume an Euler-Bernoulli beam model can thenn be presented. For the fluid element in Fig.A.2(a) balancing the forces

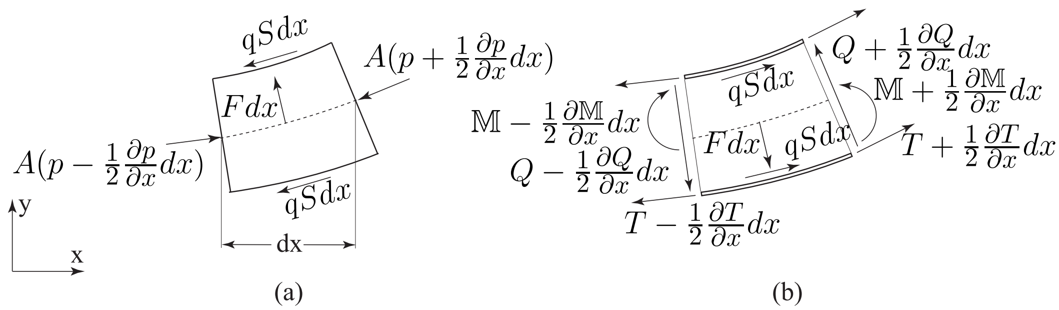

Figure A.2: Free-body diagram of (a) a fluid element and (b) its corresponding pipe element.

in the x and y directions yields the following for the fluid element:

$$-A\frac{\partial p}{\partial x} - qS - F\frac{\partial y}{\partial x} = 0 \tag{A.11}$$

$$F - A\frac{\partial}{\partial x}\left(p\frac{\partial y}{\partial x}\right) - qS\frac{\partial y}{\partial x} = M\left[\frac{\partial}{\partial t} + U\frac{\partial}{\partial x}\right]^2 y. \tag{A.12}$$

In a similar approach, balancing forces on the pipe element (see Fig.A.2(b)) yields

$$\frac{\partial T}{\partial x} + qS + F\frac{\partial y}{\partial x} - Q\frac{\partial^2 y}{\partial x^2} = 0 \tag{A.13}$$

$$\frac{\partial Q}{\partial x} - F + \frac{\partial}{\partial x}\left(T\frac{\partial y}{\partial x}\right) + qS\frac{\partial y}{\partial x} = m\frac{\partial^2 y}{\partial t^2}. \tag{A.14}$$

In Eqs.(A.11)-(A.14), A denotes the internal cross sectional area of the pipe, S denotes the internal surface area of the pipe per its unit length, p is the pressure of the fluid, q the shear stress in the fluid, and F denotes the force per unit length of the pipe normal to the pipe in the radial direction as presented in Fig.A.2(a). For the pipe element in Fig.A.2(b) Q denotes the transverse shear force, $\mathbb{M}$ denotes the bending moment of the pipe, and T denotes the tension of the pipe along its length.

In accordance with the Euler-Bernoulli beam approximation Eq.(A.13) can be simplifed by dropping the second order term, Q

$partial^2 y/\partial x^2$ to obtain

$$\frac{\partial T}{\partial x}+qS+F\frac{\partial y}{\partial x}=0. \tag{A.15}$$

Summing the forces in the axial direction for the fluid element in Eq.(A.11) and the pipe element in Eq.(A.15) yields the relationship between the tension T and the product of the pressure p and cross sectional area A

$$\frac{\partial}{\partial x}\left(T-pA\right)=0 \tag{A.16}$$

which suggests that $T-pA=0$ for $x\in[0,L]$.

To obtain the Euler-Bernoulli beam model equation, the transverse shear force Q needs to be related to the physical properties of the pipe. Starting from a general stress-stain relationship of $\sigma = E\epsilon$ where σ denotes stress, E denotes the Young's modulus, and ϵ denotes strain, the strain in the $x$direction of an Euler-Bernoulli beam can be expressed as

$$\sigma_x=-yE\frac{\mathrm{d}^2 y}{\mathrm{d}x^2}, \tag{A.17}$$

relating the axial stress to the bending moment of the pipe leads to

$$\mathbb{M}=-EI\frac{\mathrm{d}^2 y}{\mathrm{d}x^2}. \tag{A.18}$$

The transverse shear force Q is defined as

$$Q=\mathrm{d}\mathbb{M}/\mathrm{d}x, \tag{A.19}$$

which leads to the relationship between the physical pipe properties and the transverse shear force

$$Q = -EI\frac{\mathrm{d}^3 y}{\mathrm{d}x^3} \tag{A.20}$$

where E and I denotes the Young's modulus and area moment of inertia of the pipe respectively.

Combining Eqs.(A.12), (A.14), and (A.20) yields the Euler-Bernoulli beam approximation for small lateral motions [35]

$$EI\frac{\partial^4 y}{\partial x^4} + MU^2\frac{\partial^2 y}{\partial x^2} + 2MU\frac{\partial^2 y}{\partial x \partial t} + (M+m)\frac{\partial^2 y}{\partial t^2} = 0. \tag{A.21}$$

A.2 Non-Uniform Velocity Profile

In the previous section the Euler-Bernoulli beam equation was developed for a fluid-conveying pipe with a uniform velocity profile known as plug flow. Plug flow is a simple model of a velocity profile for fluid flowing in a pipe that assumes the velocity of the fluid is constant across any cross section of the pipe. It assumes that there is an infinitely thin boundary layer at the inner wall of the pipe and this greatly simplifies the analysis. When higher accuracy is desired for pipe flow analysis, a non-uniform velocity profile must be developed. The following development will first assume a triple plug flow model and then generalize it to an N-plug flow model as proposed by Hellum [23].

The triple plug flow model assumes three volumes of fluid being conveyed through the pipe, these volumes are concentric with respect to each other as well as the pipe itself. The cross section of the triple plug flow can be seen in Fig.A.3; the fluid velocity of each plug

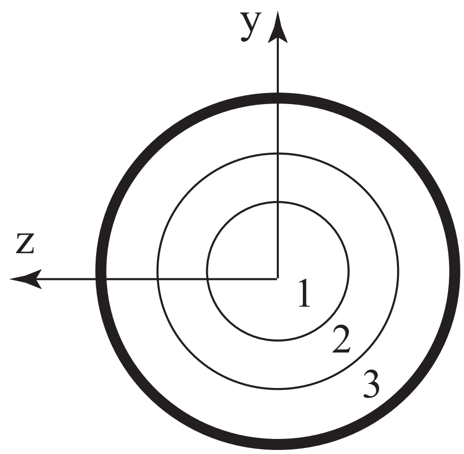

Figure A.3: Cross sectional view of three concentric fluid volumes described by triple plug flow

is constant and uniform throughout a given plug's volume, but the velocity of each plug is different. Although the triple plug flow is not physically possible, it develops the framework to introduce more plugs using the same convention. As more plugs are introduced into the model it approaches a velocity profile similar to that of a parabolic shape. The three plug flows seen in Fig.A.3 are labeled from the inside out. Fluid volume 1 exhibits a single fluid-fluid interface with volume 2, volume 2 has two fluid-fluid interfaces between fluid volumes 1 and 3, and fluid volume 3 has a single fluid-fluid interface with volume 2 and a single fluid-pipe interface with the inside surface of the fluid conveying pipe.

To proceed with an analysis similar to that of the previous section, parameters of the triple plug flow need to be defined. The cross sectional areas of fluid volumes 1, 2, and 3 will be A_1, A_2, and A_3, respectively; their flow velocities will be known as U_1, U_2, and U_3, respectively. Following the same convention, their mass per unit length will be known as M_1, M_2, and M_3. The radial force per unit length between fluid volumes 1 and 2 will be F_{12}; between fluid volumes 2 and 3 will be F_{23}; and between fluid volume 3 and the pipe will F_{3p}. Using the same convention, the shear forces at these interfaces will be denoted by

q_{12}, q_{23}, and q_{3p}. The surface area per unit length at these interfaces will be denoted by S_{12}, S_{23}, and S_{3p}. Balancing the forces in the x and y direction in Fig.A.2 yields the following equations for the fluid volumes which are similar in nature to Eqs.(A.11) and (A.12) for single plug flow.

Volume 1:

$$-A_1 \frac{\partial p}{\partial x} - q_{12} S_{12} - F_{12} \frac{\partial y}{\partial x} = 0 \tag{A.22}$$

$$F_{12} - pA_1 \frac{\partial^2 y}{\partial x^2} - q_{12} S_{12} \frac{\partial y}{\partial x} = M_1 \left[\frac{\partial}{\partial t} + U_1 \frac{\partial}{\partial x} \right]^2 y \tag{A.23}$$

Volume 2:

$$-A_2 \frac{\partial p}{\partial x} - q_{23} S_{23} + q_{12} S_{12} - (F_{23} - F_{12}) \frac{\partial y}{\partial x} = 0 \tag{A.24}$$

$$(F_{23} - F_{12}) - pA_2 \frac{\partial^2 y}{\partial x^2} - (q_{23} S_{23} - q_{12} S_{12}) \frac{\partial y}{\partial x} = M_2 \left[\frac{\partial}{\partial t} + U_2 \frac{\partial}{\partial x} \right]^2 y \tag{A.25}$$

Volume 3:

$$-A_3 \frac{\partial p}{\partial x} - q_{3p} S_{3p} + q_{23} S_{23} - \left(F_{3p} - F_{23}\right) \frac{\partial y}{\partial x} = 0 \tag{A.26}$$

$$\left(F_{3p} - F_{23}\right) - pA_3 \frac{\partial^2 y}{\partial x^2} - \left(q_{3p} S_{3p} - q_{23} S_{23}\right) \frac{\partial y}{\partial x} = M_3 \left[\frac{\partial}{\partial t} + U_3 \frac{\partial}{\partial x} \right]^2 y \tag{A.27}$$

Similar to Eqs.(A.13) and (A.14) for single plug flow, balancing the forces for triple plug flow yields the equations for the pipe

$$\frac{\partial T}{\partial x} + q_{3p}S_{3p} + F_{3p}\frac{\partial y}{\partial x} - Q\frac{\partial^2 y}{\partial x^2} = 0 \tag{A.28}$$

$$\frac{\partial Q}{\partial x} - F_{3p} + \frac{\partial}{\partial x}\left(T\frac{\partial y}{\partial x}\right) + q_{3p}S_{3p}\frac{\partial y}{\partial x} = m\frac{\partial^2 y}{\partial t^2} \tag{A.29}$$

Summing Eqs.(A.22), (A.24), (A.26), and (A.28) in the x direction yields

$$-\left(A_1 + A_2 + A_3\right)\frac{\partial p}{\partial x} + \frac{\partial T}{\partial x} = 0 \tag{A.30}$$

where $(A_1 + A_2 + A_3) = A$ the total inner cross sectional area of the pipe. Noting that A is not a function of x, Eq.(A.30) can be expressed as

$$\frac{\partial}{\partial x}\left(T - pA\right) = 0 \tag{A.31}$$

which is identical to Eq.(A.16) developed for single plug flow by Païdoussis [35]. Summing the equations in the y direction, Eqs.(A.23), (A.25), (A.27), and (A.29) yields

$$-pA\frac{\partial^2 y}{\partial x^2} + \frac{\partial Q}{\partial x} + T\frac{\partial^2 y}{\partial x^2} = \sum_{n=1}^{3} M_n\left[\frac{\partial}{\partial t} + U_n\frac{\partial}{\partial x}\right]^2 y + m\frac{\partial^2 y}{\partial t^2}. \tag{A.32}$$

Following the previous derivation for single plug flow, the Euler-Bernoulli beam approximation for triple plug flow can be obtained with the substitutions of $(T - pA) = 0$ and $Q = -EI(\partial^3 y/\partial x^3)$ into Eq.(A.32):

$$EI\frac{\partial^4 y}{\partial x^4} + \left(\sum_{n=1}^{3} MnU_n^2\right)\frac{\partial^2 y}{\partial x^2} + 2\left(\sum_{n=1}^{3} MnUn\right)\frac{\partial^2 y}{\partial x \partial t} + \left(m + \sum_{n=1}^{3} Mn\right)\frac{\partial^2 y}{\partial t^2} = 0 \tag{A.33}$$

A continuous solution of the Euler-Bernoulli beam approximation can be found by increasing the number of fluid volumes from 3 to N with additional volumes similar to that of volume 2, which include two fluid-fluid interfaces. The additional volumes do not complicate the analysis since the additional fluid-fluid interactions terms are canceled when summing the equations in the x and y directions just as they did with triple plug flow in Eqs.(A.30) and (A.32). Thus the Euler-Bernoulli beam approximation for triple plug flow, Eq.(A.33) can be rewritten as

$$EI\frac{\partial^4 y}{\partial x^4} + \left(\sum_{n=1}^{N} MnU_n^2\right)\frac{\partial^2 y}{\partial x^2} + 2\left(\sum_{n=1}^{N} MnUn\right)\frac{\partial^2 y}{\partial x \partial t} + \left(m + \sum_{n=1}^{N} Mn\right)\frac{\partial^2 y}{\partial t^2} = 0 \quad \text{(A.34)}$$

where N is any integer greater than 3. As N approaches ∞, the thickness of each plug approaches 0 and the summations of Eq.(A.34) can be replaced with integrals. The average velocity of the fluid can be expressed as

$$\bar{U} = \frac{1}{A}\iint_A U(A)\mathrm{d}A, \quad \text{(A.35)}$$

where the area A is the inside of the pipe. For a pipe with an internal radius R, the average velocity of the fluid inside the pipe can be expressed as

$$\bar{U} = \frac{2}{R^2}\int_0^R U(r)r\mathrm{d}r. \quad \text{(A.36)}$$

Note that M_n is the mass per unit length for each volume, thus $\sum_{n=1}^{N} Mn = M$. The terms of the Euler-Bernoulli beam approximation for N plug flow as $N \to \infty$ can be expressed as

$$\left(\sum_{n=1}^{N} MnU_n^2\right) = \rho_f \iint_A U^2(A)\mathrm{d}A = 2\pi\rho_f \int_0^R U^2(r)r\mathrm{d}r = \mu M\bar{U}^2,$$

$$2\left(\sum_{n=1}^{N} MnU_n^2\right) = 2\rho_f \iint_A U(A)\mathrm{d}A = 2\rho_f A\bar{U} = 2M\bar{U},$$

$$\left(m + \sum_{n=1}^{N} Mn\right) = m + M, \tag{A.37}$$

where ρ_f is the density of the conveyed fluid and μ is the non-dimensional momentum correction factor. The momentum correction factor is an artifact of the conveying geometry and the fluid velocity profile $U(r)$, for the case of a fluid conveying pipe, the momentum correction factor is

$$\mu = \frac{2}{R^2}\int_0^R \left[\frac{U(r)}{\bar{U}}\right]^2 r\mathrm{d}r. \tag{A.38}$$

Substituting the algebraic simplifications found in Eq.(A.37) into Eq.(A.34) the Euler-Bernoulli beam approximation can be expressed as

$$EI\frac{\partial^4 y}{\partial x^4} + \mu M\bar{U}^2\frac{\partial^2 y}{\partial x^2} + 2M\bar{U}\frac{\partial^2 y}{\partial x \partial t} + (M+m)\frac{\partial^2 y}{\partial t^2} = 0 \tag{A.39}$$

which shares the same form as the Euler-Bernoulli beam equation for single plug flow as expressed by Eq.(A.21). Notice that for a uniform velocity profile, $\mu = 1$, and Eq.(A.21) and (A.39) are identical.

Hellum et al. [23] went on further to provide the solution of the differential equation to analyze the behavior a fluid-conveying pipe by introducing the familiar boundary conditions for a cantilever

$$y(0,t)=0,\;\; y_x(0,t)=0,\;\; y_{xx}(L,t)=0,\;\; y_{xxx}(L,t)=0, \tag{A.40}$$

where y_x, y_{xx}, and y_{xxx} are the first, second, and third partial derivatives of y with respect to x respectively. With the following change of variables the equation of motion is non-dimensionalized

$$Y=\frac{y}{L},\;\; X=\frac{x}{L},\;\; T=t\Omega.$$

The non-dimensional velocity of the fluid can be expressed as

$$u=\left(\frac{M}{EI}\right)^{1/2}\bar{U}L,$$

the mass fraction as

$$\beta=\frac{M}{m+M},$$

and the frequency as follows:

$$\omega=\left(\frac{M+m}{EI}\right)^{1/2}\Omega L^2.$$

If the solution is assumed to be separable such that

$$Y(X,T)=\phi(X)e^{-i\omega T}, \tag{A.41}$$

it is then then possible to produce the non-dimensional equation of motion and the corresponding boundary conditions

$$\frac{\mathrm{d}^4\phi}{\mathrm{d}X^4} + \mu u^2 \frac{\mathrm{d}^2\phi}{\mathrm{d}X^2} + 2\beta^{1/2} u i\omega \frac{\mathrm{d}\phi}{\mathrm{d}X} - \omega^2 \phi = 0, \tag{A.42}$$

$$\phi(0) = 0,\ \ \phi_X(0),\ \ \phi_{XX}(1) = 0,\ \ \phi_{XXX}(1) = 0, \tag{A.43}$$

where ϕ_x, ϕ_{xx}, and ϕ_{xxx} are the first, second, and third partial derivatives of ϕ respectively. Assuming the solution of ϕ to be of the form of

$$\phi(X) = Ae^{zX}$$

yields the characteristic polynomial

$$z^4 + \mu u^2 z^2 + 2\beta^{1/2} u i\omega z - \omega^2 = 0. \tag{A.44}$$

For specific values of μ, u, and β which are obtained by the physical parameters of the fluid-conveying pipe Eq.(A.44) provides four roots, $z_n, n = 1, 2, 3, 4$, where $z_n = z_n(\omega)$. The complete solution of $\phi(X)$ has the form of

$$\phi(X) = A_1 e^{z_1 X} + A_2 e^{z_2 X} + A_3 e^{z_3 X} + A_4 e^{z_4 X}. \tag{A.45}$$

The solution of Eq.(A.45) based on the boundary conditions presented in Eq.(A.43) results in the complete solution

$$Y(X,T) = \sum_{n=1}^{4} A_n e^{z_n X} e^{i\omega T} = \sum_{n=1}^{4} A_n \underbrace{e^{\Re[Z_n]X}}_{\text{(i)}} \underbrace{e^{i(\Im[Z_n]X + \Re[\omega]T)}}_{\text{(ii)}} \underbrace{e^{-\Im[\omega]T}}_{\text{(iii)}}. \tag{A.46}$$

Inspecting the above equation indicates that $Y(X,T)$ is a product of three exponential terms, (i), (ii) and (iii). The first term, $e^{\Re[Z_n]X}$ is bounded since X is bounded. The second term, $e^{i(\Im[Z_n]X+\Re[\omega]T)}$ is oscillatory from its imaginary exponent. The third term, $e^{-\Im[\omega]T}$ can grow unbounded with time if $\Im[\omega] < 0$ which represents the unstable dynamics of the pipe. The exact mode and the velocity at which the fluid-conveying pipe becomes unstable depends on the fluid mass fraction β which is explained in detail in [23].

BIBLIOGRAPHY

BIBLIOGRAPHY

[1] J Aitken. XIV. An account of some experiments on rigidity produced by centrifugal force. *Philosophical Magazine Series 5*, 5(29):81–105, 1878.

[2] H Ashley and G Haviland. Bending vibrations of a pipe line containing flowing fluid. *Journal of Applied Mechanics*, 17(3):229–232, 1950.

[3] AK Bajaj, PR Sethna, and TS Lundgren. Hopf bifurcation phenomena in tubes carrying a fluid. *SIAM Journal on Applied Mathematics*, 39(2):213–230, 1980.

[4] DS Barrett, MS Triantafyllou, DKP Yue, MA Grosenbaugh, and MJ Wolfgang. Drag reduction in fish-like locomotion. *Journal of Fluid Mechanics*, 392:183–212, 1999.

[5] TB Benjamin. Dynamics of a system of articulated pipes conveying fluid. I. Theory. *Proceedings of the Royal Society of London. Series A. Mathematical and Physical Sciences*, 261(1307):457, 1961.

[6] TB Benjamin. Dynamics of a system of articulated pipes conveying fluid. I. Theory. *Proceedings of the Royal Society of London. Series A. Mathematical and Physical Sciences*, 261(1307):457, 1961.

[7] FJ Bourrieres. Sur un phénomene doscillation auto-entretenue en mécanique des fluides réels Publications Scientifiques et Techniques du Ministeres de lAir 147, 1939.

[8] JM Brunnschweiler. Water-escape velocities in jumping blacktip sharks. *Journal of the Royal Society Interface*, 2(4):389, 2005.

[9] Z Chen, S Shatara, and X Tan. Modeling of biomimetic robotic fish propelled by an ionic polymer–metal composite caudal fin. *Mechatronics, IEEE/ASME Transactions on*, 15(3):448–459, 2010.

[10] B Collipp and M Hall. 7,500 Ft: A New Record Deepwater Drilling Program. In *Offshore Technology Conference*, 1984.

[11] Atmel Corporation. 8-bit avr microcontroller with 128k bytes in-system programmable flash, July 2010.

[12] VP Feodos.ev. Vibrations and stability of a pipe when liquid flows through it. *Inzhenernyi Sbornik*, 10:169–170, 1951.

[13] FE Fish. The myth and reality of Gray's paradox: implication of dolphin drag reduction for technology. *Bioinspiration & Biomimetics*, 1:R17, 2006.

[14] B Fletcher, A Bowen, DR Yoerger, and LL Whitcomb. Journey to the Challenger Deep: 50 Years Later With the Nereus Hybrid Remotely Operated Vehicle. *Marine Technology Society Journal*, 43(5):65–76, 2009.

[15] L Freitag, M Grund, S Singh, J Partan, P Koski, and K Ball. The WHOI micro-modem: an acoustic communications and navigation system for multiple platforms. In *OCEANS, 2005. Proceedings of MTS/IEEE*, pages 1086–1092. IEEE, 2005.

[16] J Gray. Studies in animal locomotion. VI. The propulsive powers of the dolphin. *J. exp. Biol*, 13:192–199, 1936.

[17] RW Gregory and MP Païdoussis. Unstable oscillation of tubular cantilevers conveying fluid. I. Theory. *Proceedings of the Royal Society of London. Series A. Mathematical and Physical Sciences*, 293(1435):512, 1966.

[18] RW Gregory and MP Païdoussis. Unstable oscillation of tubular cantilevers conveying fluid. II. Experiments. *Proceedings of the Royal Society of London. Series A. Mathematical and Physical Sciences*, 293(1435):528, 1966.

[19] MJ Hannoyer and MP Païdoussis. Instabilities of tubular beams simultaneously subjected to internal and external axial flows. *ASME Journal of mechanical design*, 100:328–336, 1978.

[20] KA Harper, MD Berkemeier, and S Grace. Modeling the dynamics of spring-driven oscillating-foil propulsion. *Oceanic Engineering, IEEE Journal of*, 23(3):285–296, 2002.

[21] RK Heller and MB Head. Accomplishments of the Cable-Controlled Underwater Research Vehicle. In *Symposium on Modern Developments in Marine Sciences: papers*

CM Wong, Symposium Committee general chairman and others, page 169. Western Periodicals Co., 1966.

[22] A Hellum, R Mukherjee, and AJ Hull. Flutter instability of a fluid-conveying fluid-immersed pipe affixed to a rigid body. *Journal of Fluids and Structures*, 2011.

[23] AM Hellum, R Mukherjee, and AJ Hull. Dynamics of pipes conveying fluid with non-uniform turbulent and laminar velocity profiles. *Journal of fluids and structures*, 26(5):804–813, 2010.

[24] G Herrmann. Stability of equilibrium of elastic systems subjected to non-conservative forces, Appl. *Mech. Revs*, 20(2):103–108, 1967.

[25] G Herrmann and S Nemat-Nasser. Instability modes of cantilevered bars induced by fluid flow through attached pipes* 1. *International Journal of Solids and Structures*, 3(1):39–52, 1967.

[26] PJ Holmes. Pipes supported at both ends cannot flutter. *Journal of Applied Mechanics*, 45:619, 1978.

[27] GW Housner. Bending vibrations of a pipe line containing flowing fluid. *Journal of Applied Mechanics*, 19(2):205–208, 1952.

[28] MJ Lighthill. Note on the swimming of slender fish. *Journal of Fluid Mechanics*, 9(02):305–317, 1960.

[29] RH Long. Experimental and theoretical study of transverse vibration of a tube containing flowing fluid. *Journal of Applied Mechanics*, 22(1):65–68, 1955.

[30] TS Lundgren, PR Sethna, and AK Bajaj. Stability boundaries for flow induced motions of tubes with an inclined terminal nozzle. *Journal of Sound and Vibration*, 64(4):553–571, 1979.

[31] S Nemat-Nasser, SN Prasad, and G Herrmann. Destabilizing effect of velocity-dependent forces in nonconservative continuous systems. *AIAA J*, 4(7):1276–1280, 1966.

[32] JB Newman and D Stakes. Tiburon: Development of an ROV for ocean science research. In *OCEANS'94.'Oceans Engineering for Today's Technology and Tomorrow's Preservation.'Proceedings*, volume 2, pages II–483. IEEE, 1994.

[33] FI Niordson. *Vibrations of a cylindrical tube containing flowing fluid*. Elanders Boktr., 1953.

[34] MP Païdoussis. Dynamics of tubular cantilevers conveying fluid. *ARCHIVE: Journal of Mechanical Engineering Science 1959-1982 (vols 1-23)*, 12(2):85–103, 1970.

[35] MP Païdoussis. *Fluid-Structure Interactions, Vol 1: Slender Structures and Axial Flow*. San Diego, CA: Academic Press Inc, 1998.

[36] MP Païdoussis and EB Deksnis. Articulated models of cantilevers conveying fluid: the study of a paradox. *ARCHIVE: Journal of Mechanical Engineering Science 1959-1982 (vols 1-23)*, 12(4):288–300, 1970.

[37] MP Païdoussis and NT Issid. Dynamic stability of pipes conveying fluid. *Journal of Sound and Vibration*, 33(3):267–294, 1974.

[38] MP Païdoussis and BE Laithier. Dynamics of Timoshenko beams conveying fluid. *ARCHIVE: Journal of Mechanical Engineering Science 1959-1982 (vols 1-23)*, 18(4):210–220, 1976.

[39] EK Ritter and JM Brunnschweiler. Do Sharksuckers, Echeneis Naucrates, Induce Jump Behaviour in Blacktip Sharks, Carcharhinus Limbatus ? *Marine and Freshwater Behaviour and Physiology*, 36(2):111–113, 2003.

[40] CH Robotics. Chr-6dm attitude and heading reference system, August 2012.

[41] ON Semiconducto. 5.0 a, step.up/down/inverting switching regulators, November 2005.

[42] PC Strefling, AM Hellum, and R Mukherjee. Modeling, Simulation, and Performance of a Synergistically Propelled Ichthyoid. *Mechatronics, IEEE/ASME Transactions on*, 2011. (In Submission).

[43] PC Strefling, AM Hellum, and R Mukherjee. Performance of a Synergistically Propelled Ichthyoid [SPI]:Simulation and Experimental Results. In *Dynamic Systems and Control*. ASME, 2011.

[44] PC Strefling, AM Hellum, and R Mukherjee. Performance of a Synergistically Propelled Ichthyoid [SPI]:Simulation and Experimental Results. In *International Conference on Intelligent Robots and Systems*. ASME, 2011.

[45] H Talkington. Manned and remotely operated submersible systems: a comparison. Technical report, NAVAL UNDERSEA CENTER SAN DIEGO CA, 1976.

[46] X Tan, W Xi, and JS Baras. Decentralized coordination of autonomous swarms using parallel Gibbs sampling. *Automatica*, 2010.

[47] MS Triantafyllou, GS Triantafyllou, and DKP Yue. Hydrodynamics of fishlike swimming. *Annual review of fluid mechanics*, 32(1):33–53, 2000.

[48] PV y Alvarado and K Youcef-Toumi. Design of machines with compliant bodies for biomimetic locomotion in liquid environments. *Journal of Dynamic Systems, Measurement, and Control*, 128:3, 2006.